

Analysis Note

Direct virtual photon production in Au+Au
collisions at $\sqrt{s_{NN}}=200$ GeV at RHIC

Chi Yang

March, 23th 2015

TABLE OF CONTENTS

0.1	Data Set and Event Selection	1
0.2	Electron Identification	3
0.3	Pair Reconstruction	6
0.3.1	Background study	8
0.3.2	Raw signal	16
0.4	Efficiency and Acceptance	16
0.4.1	Single track efficiency	18
0.4.2	Pair efficiency	23
0.4.3	Acceptance	26
0.5	Cocktail Simulation	27
0.5.1	Light flavor meson contribution	27
0.5.2	Heavy flavor contribution	33
0.6	Di-electron Signal	34
0.6.1	Di-electron continuum in high p_T	35
0.7	Direct Virtual Photon Production	38
0.7.1	Direct virtual photon and the associated e^+e^- pairs	38
0.7.2	Excess in low-mass region	39
0.7.3	Fraction of the direct virtual photon	40
0.7.4	Direct virtual photon invariant yield	44
0.8	Systematic Uncertainty	46
0.8.1	Uncertainty from di-electron continuum	46
0.8.2	Uncertainty from the fitting method	50

LIST OF FIGURES

0.1 Reference multiplicity distribution for Run11 200GeV Au+Au data after event topological cuts.	2
0.2 Vertex Z (left) and magnetic field (right) distribution for Run11 200GeV Au+Au data after event topological cuts.	3
0.3 The distribution of $n\sigma_e$ and $1/\beta$ as a function of momentum. Panel a): $n\sigma_e$ vs. p . Panel b): $1/\beta$ vs. p . The bands from different particles species are marked in the plots.	5
0.4 The $n\sigma_e$ as a function of momentum distribution after $1/\beta$ cut. The range between red lines is selected.	5
0.5 Electron purity from Run11 data. Left panel: fitting on $n\sigma_e$ distribution. The red curve is the electron contribution while the blue one comes from contamination. The pink curve is the overall fit function. Right panel: electron purity as a function of momentum.	6
0.6 Purity for TPC+EMC electrons.	7
0.7 Purity fitting plots for TPC+EMC electrons in different p_T slices.	7
0.8 Invariant mass (M_{ee}) distribution of random combination on e^+e^- pair in same event as a function of p_T with Run11 data.	8
0.9 Di-electron signals (M_{ee} vs p_T) with like-sign background reconstruction method for Run11 data.	10
0.10 The event-plane distribution for Run11 data.	11
0.11 Di-electron signals (M_{ee} vs p_T) with mixed-event method with Run11 data. .	12
0.12 A diagram for ϕ_V definition.	13
0.13 Simulation on ϕ_V distribution of gamma conversion in different p_T slices. .	14

0.14 ϕ_V cut efficiency based on the pion simulation results. This efficiency is used as the ϕ_V cut efficiency on signal (after gamma rejection). The difference between virtual photon simulation and this pion simulation is taken as the systematic uncertainty from ϕ_V cut.	15
0.15 The distribution of M_{ee} difference (global mass - primary mass) as a function of global mass.	15
0.16 The distribution of M_{ee} with different reconstruction methods for Run10 data.	16
0.17 The distribution of M_{ee} with different reconstruction methods for Run11 data.	17
0.18 The di-electron raw signal for Run10 data. Left panel: in low mass region w/o number of events and bin width correction. Right panel: w/ number of events and bin width correction.	17
0.19 The di-electron raw signal for Run11 data. Left panel: in low mass region w/o number of events and bin width correction. Right panel: w/ number of events and bin width correction.	17
0.20 Signal over background ratio with likesign method. Left panel: Run10 data. Right panel: Run11 data.	18
0.21 ϕ dependence of TPC tracking efficiency. Upper panels: Run10. Lower panels: Run11.	19
0.22 TPC tracking efficiency for Run10 and Run11. Blue: Run10. Red: Run11.	20
0.23 $nHitsDedx$ cut efficiency for Run11.	20
0.24 η and ϕ dependence of TOF matching efficiency for Run11 π^+	21
0.25 TOF matching efficiencies of different particle species for Run10 and Run11. Left panel: Run10. Right panel: Run11.	22

0.26 Electron $1/\beta$ distribution for Run11 data. The red lines are the upper and lower cut edges. The red markers are the Gaussian fit means in different momentum slices. The blue line is the fitting result on these fit means for Run10 data.	22
0.27 Left panel: Gaussian fit on $1/\beta$ distribution in a momentum slice for Run11. Middle panel: Run11 $1/\beta$ cut efficiency. Right panel: Run10 $1/\beta$ cut efficiency.	23
0.28 $n\sigma_e$ cut efficiencies for Run10 and Run11. Upper panels: Run10. Lower panels: Run11. Left panels: $n\sigma_e$ cut efficiency. Right panels: $n\sigma_e$ distribution of the photonic electron sample.	24
0.29 TPC tracking efficiency correction factors for different centralities. Left : Run10. Right : Run11. From upper to lower : 40-80%, 10-40%, 0-10% centralities.	24
0.30 TOF matching efficiency correction factors for different centralities for Run11.	25
0.31 ndEdx points efficiency correction factors for different centralities. Left : Run10. Right : Run11. From upper to lower : 40-80%, 10-40%, 0-10% centralities.	25
0.32 Di-electron pair detection efficiencies without ϕ_V cut efficiency in different p_T slices from Run11 Au+Au at 200 GeV.	26
0.33 STAR acceptance in mid-rapidity for di-electron detection based on cocktail simulation (<i>cocktail acc / cocktail mc</i>).	27
0.34 The distribution (M_{ee} vs p_T , vs p_T) of acceptance difference between unlike-sign and like-sign ee pair for Run10 and Run11. Left panels: Run10. Right panels: Run11.	28
0.35 The Tsallis Blast-Wave model fitting for meson sources which are involved in cocktail simulation. The meson production are from published results in Au+Au at 200 GeV.	30

0.36 Cocktails for different acceptance settings and Run11 efficiency weighting..	30
0.37 Meson to π^0 ratio for our centrality dependence cocktail simulation inputs for different mesons in 0-10% centrality	31
0.38 Meson to π^0 ratio for our centrality dependence cocktail simulation inputs for different mesons in 10-40% centrality	32
0.39 Meson to π^0 ratio for our centrality dependence cocktail simulation inputs for different mesons in 40-80% centrality	32
0.40 dN/dy input for cocktail simulation	33
0.41 The cocktail within STAR acceptance in Au+Au at 200GeV.	34
0.42 The di-electron continuum from Run10 and Run11 compared to cocktail with different contributions.	35
0.43 The combined di-electron continuum of Run10 and Run11 as a function of p_T in different centralities. Upper left : 0-80%. Upper right : 0-10%. Lower left : 10-40%. Lower right : 40-80%.	36
0.44 The difference between Run10 and Run11 signals as a function of p_T in different centralities. Upper left : 0-80%. Upper right : 0-10%. Lower left : 10-40%. Lower right : 40-80%.	37
0.45 Left panel: Single electron efficiency TPC+EMC. Right panel: Pair detec- tion efficiency in high p_T range (5-10GeV/c).	38
0.46 The $L(M_{ee})/M_{ee}$ shapes smeared by the STAR acceptance. The p_T depen- dence of STAR acceptance can be observed in low p_T	41
0.47 The two component function fit on Run10 and Run11 combined Au+Au di-electron continuum in $0.1 < M_{ee} < 0.28$ GeV/ c^2 at 200GeV. The bottom panels are the ratio of data points versus fit fuction and the data points versus normalized cocktail.	42

0.48 The two component function fit on Run11 Au+Au di-electron continuum in $0.1 < M_{ee} < 0.28 \text{ GeV}/c^2$ at 200GeV with EMC triggered events in high p_T . The errors shown are the quadrature sum of statistical and systematic errors. The bottom panels are the ratio of data points versus fit fuction and the data points versus normalized cocktail.	43
0.49 The fraction of direct virtual photon compared with the NLO pQCD prediction. The curves represent $T_{AA}d\sigma_\gamma^{NLO}(p_T)/dN_\gamma^{inclusive}(p_T)$. The red and blue curves corresponds to the theory scale $\mu = 0.5p_T, 1.0p_T$, respectively, showing the scale dependence of the theory.	44
0.50 The invariant yield of direct virtual photon in 0-80%. The pink dashed curve represents a power-law fit to PHENIX 200GeV $p + p$ cross section, scaled by T_{AA} . Right panel shows the direct virtual photon invariant yield compared to model predictions including the contributions from different sources.	45
0.51 The invariant yield of direct virtual photon. The pink dashed curve represents a power-law fit to PHENIX 200GeV $p + p$ cross section, scaled by T_{AA} . Left: 0-10%. Middle: 10-40%. Right: 40-80%.	46
0.52 Centrality dependence of the direct photon invariant yields as a function of p_T in Au+Au collisions at $\sqrt{s_{NN}} = 200 \text{ GeV}$. The solid curve represents a power-law fit to PHENIX 200 GeV $p + p$ cross section, scaled by T_{AA} , including a green band which explain the uncertainty contributed from fitting and T_{AA} scale. The error bars and boxes represent the statistical and systematic uncertainties, respectively.	47
0.53 The direct photon invariant yields as a function of p_T in Au+Au collisions at $\sqrt{s_{NN}} = 200 \text{ GeV}$ compared to model predictions from Rapp et al. and Paquet et al. . The statistical and systematic uncertainties are shown by the bars and boxes, respectively.	48

0.54 The comparison of the data from STAR, PHENIX, and the theoretical model calculations. Panel (a) is the excess yield, which is the direct photon yield with the N_{coll} scaled p+p contribution subtracted, in comparison with the thermal component contributions in the model calculations.	49
0.55 Uncertainty contribution from fit range. Left: 0-80%. Right: 0-10%	51
0.56 The p_T distributions from different sets compared to the default value for η source in cocktail simulation.	52
0.57 The relative uncertainty and its contributed sources. Left: 0-80%. Right: 0-10%	53
0.58 The relative uncertainty and its contributed sources. Left: 10-40%. Right: 40-80%	53

LIST OF TABLES

0.1	Centrality definition on Run10 and Run11 200 GeV Au+Au collisions.	1
0.2	Event selection cuts.	2
0.3	Track quality cuts.	4
0.4	Branch ratio and rapidity densities (dN/dy) for different sources in the cocktail simulation.	31
0.5	Track quality cuts for EMC triggered data.	37
0.6	Systematic uncertainties from different sources in 0-80%.	53
0.7	Systematic uncertainties from different sources in 0-10%.	54
0.8	Systematic uncertainties from different sources in 10-40%.	54
0.9	Systematic uncertainties from different sources in 40-80%.	55

Table 0.1: Centrality definition on Run10 and Run11 200 GeV Au+Au collisions.

centrality	Run10	Run11
0 - 10%	> 379	> 396
10 - 20%	> 269	> 281
20 - 30%	> 184	> 193
30 - 40%	> 119	> 125
40 - 50%	> 73	> 76
50 - 60%	> 41	> 43
60 - 70%	> 21	> 22
70 - 80%	> 10	> 10

0.1 Data Set and Event Selection

In Run10 and Run11, STAR took 200 GeV Au+Au minimum bias (MB) data which were triggered by VPD and ZDC coincidence. Tab. 0.1 is the centrality definition for Run10 and Run11 200 GeV Au+Au MB data. The final centrality used in this analysis is based on the StRefMultCorr class.

Events in 0-80% centrality range called MB events are selected for this analysis. To improve the quality of these events, some event selection cuts in Tab. 0.2 are applied in the analysis. To ensure that the events are measured in a uniform acceptance range, 30 cm cut on vertex Z is applied. The cut on $|Vz - VpdVz|$ and Vr is to reject the pile up events caused by the high interaction rate. Vz is the Z position of the vertex measured by the TPC tracking information while $VpdVz$ is the Z position of VPD measured vertex. After all event selection cuts and bad run rejection, there are 258M and 488M events left for Run10 and Run11, respectively. Fig. 0.1 shows the reference multiplicity distribution for the events passed all the events topological cuts ($|Vz - VpdVz|$, Vr , Vz and none zero vertex cuts). Fig. 0.2 show the vertex Z and magnetic field distributions with this setting.

Table 0.2: Event selection cuts.

Item	Cut
$ Vz $	$\leq 30\text{cm}$
$ Vz - VpdVz $	$\leq 3\text{cm}$
$ Vr $	$\leq 2\text{cm}$
$ Vx $	$\geq 1\text{e-5 cm}$
$ Vy $	$\geq 1\text{e-5 cm}$
$ Vz $	$\geq 1\text{e-5 cm}$

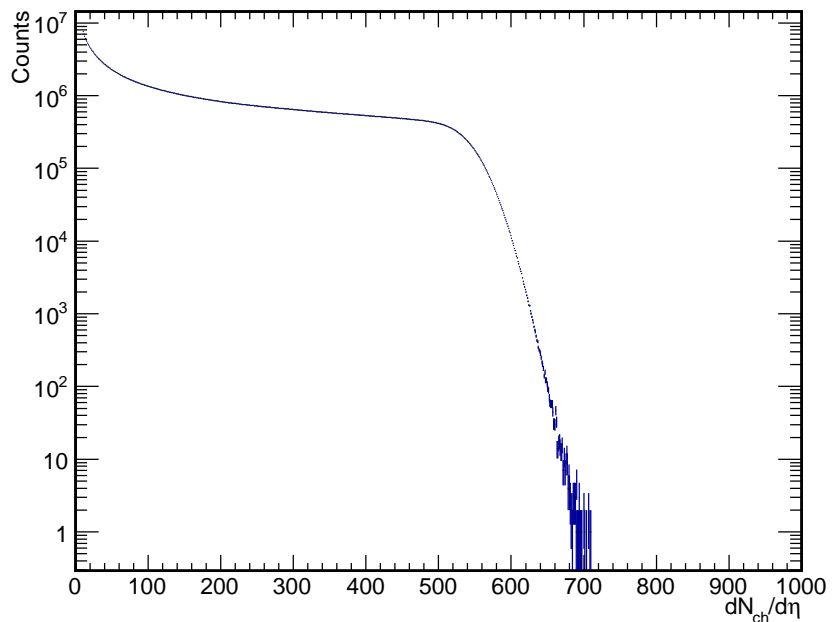


Figure 0.1: Reference multiplicity distribution for Run11 200GeV Au+Au data after event topological cuts.

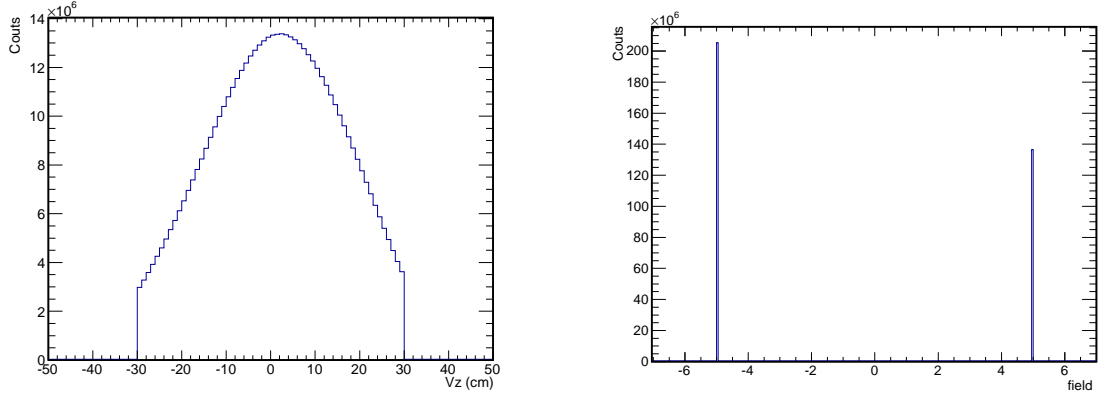


Figure 0.2: Vertex Z (left) and magnetic field (right) distribution for Run11 200GeV Au+Au data after event topological cuts.

0.2 Electron Identification

To identify electrons from hadrons, a combination of TPC and TOF information is required. With the cut of the velocity of particles very close to speed of light, the energy loss dE/dx can be used to identify the electrons. The dE/dx of charged particles passing material can be described by the Bethe-Bloch formula. A factor $n\sigma_P$ (Eq. 0.1) is defined in the data production and used in the analysis to identify the particles by the difference between their measured dE/dx and expected values more conveniently. The P in the equation stands for a specific particle. $(dE/dx)_{Measured}$ is the TPC measured energy loss while $(dE/dx)_{PBichsel}$ is the expected dE/dx value of Bichsel function. R is the resolution of TPC dE/dx .

$$n\sigma_P = \log\left[\frac{(dE/dx)_{Measured}}{(dE/dx)_{PBichsel}}\right]/R \quad (0.1)$$

To improve the quality of tracks, some track quality cuts shown in Tab. 0.3 are applied. The detail effects of these track cuts are :

1. p_T cut: Minimum p_T that a track can pass TPC.
2. η cut: Coverage of TPC.
3. *Global dca*: To reject tracks from secondary vertex decay.

Table 0.3: Track quality cuts.

Item	Cut
p_T	$\geq 0.2 \& \leq 50 GeV/c$
$ \eta $	≤ 1
<i>Global dca</i>	$\leq 1 cm$
$nHitsFit$	≥ 20
$nHitsDedx$	≥ 16
$nHitsFit/nHitsMax$	≥ 0.52
$ y_{local} $	$\leq 1.8 cm$
$PairY$	≤ 1
$ 1/\beta - 1/\beta_{fitmean} $	$\leq 0.03 (1/\beta_{fitmean} _{p>2} = 1/\beta_{fitmean} _{p=2})$
$n\sigma_e$	$\leq 2.0 \& \geq f(p)$ (Run10)
$n\sigma_e$	$\leq (2.0 - 0.4) \& \geq (f(p) - 0.4)$ (Run11)
$f(p) = -2.3 + 1.5p$	

4. $nHitsFit$: More points for track reconstruction, improve the track reconstruction precision.
5. $nHitsDedx$: More points in dE/dx measurement, improve dE/dx precision.
6. $nHitsFit/nHitsMax$: To reject double counting when reconstructing tracks.
7. $|y_{local}|$: The relative Y direction position of TOF hit to the center of the readout pad, improve β precision.

The β and $n\sigma_e$ related cuts in the table are the key EID cuts. Seen from Fig. 0.3 panel *a*) which shows the $n\sigma_e$ distribution of Run11 data, the electron band is overlapped with other charged hadrons. Panel *b*) is the distribution of $1/\beta$. With a $1/\beta$ cut applied, the $n\sigma_e$ distribution will be converted to as shown in Fig. 0.4. The slow hadrons have been rejected. The electron band is clearly shown while there are still some contaminations from hadrons. That is caused by mismatching of time-of-flight and TPC tracking information. An $n\sigma_e$ cut shown as red lines is applied. The tracks between red lines are selected as electron candidates. For TPC calibration reason, the mean value of $n\sigma_e$ shifts about -0.4 in Run11. The $n\sigma_e$ cuts for Run10 and Run11 are different in order to select more good candidates. The efficiencies of these EID cuts will be discussed in Sec. 0.4.1.

To calculate the electron purity, two Gaussian fits are used to fit the $n\sigma_e$ distribution

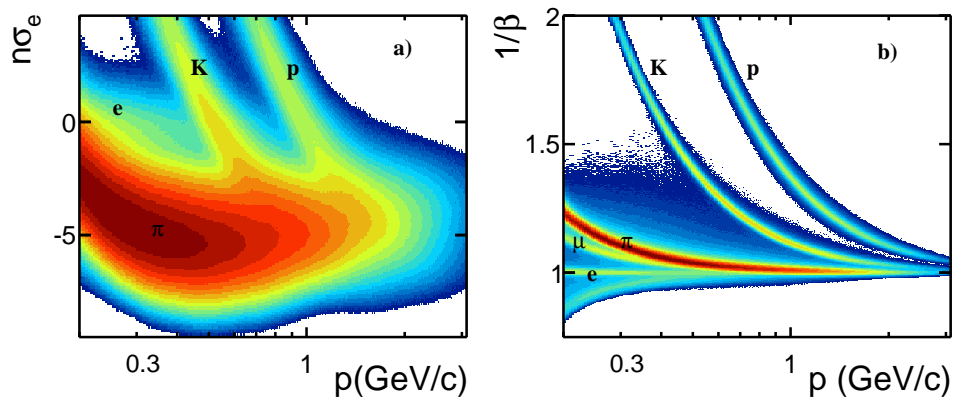


Figure 0.3: The distribution of $n\sigma_e$ and $1/\beta$ as a function of momentum. Panel a): $n\sigma_e$ vs. p . Panel b): $1/\beta$ vs. p . The bands from different particles species are marked in the plots.

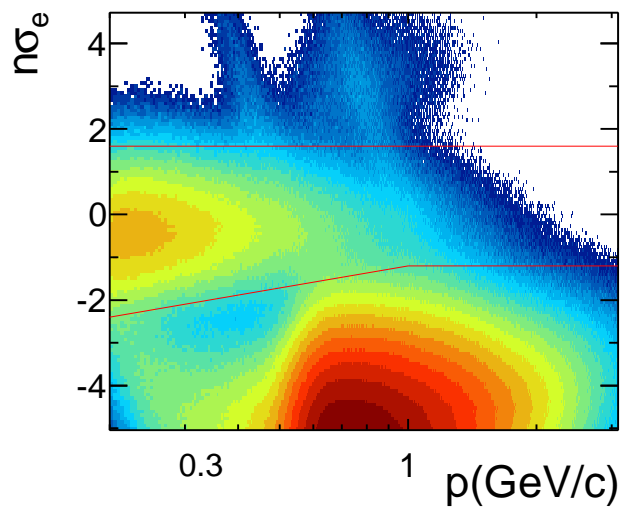


Figure 0.4: The $n\sigma_e$ as a function of momentum distribution after $1/\beta$ cut. The range between red lines is selected.

after EID cuts. As shown in the left panel of Fig. 0.5, the red curve shows the electron distribution while the blue curve is the contamination from hadron. The ratio of the electron counts represented by the red curve versus the overall value in the same $n\sigma_e$ cut range is defined as the purity. The right panel of the plot shows the purity as a function of momentum.

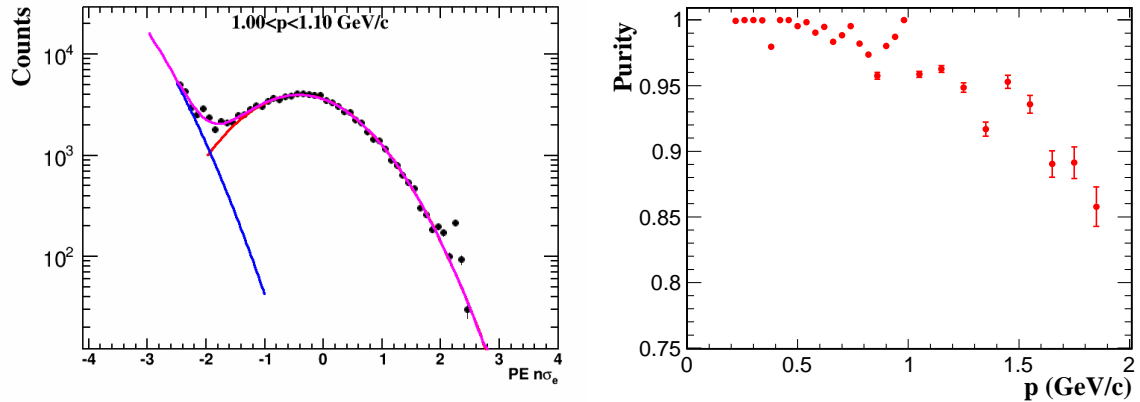


Figure 0.5: Electron purity from Run11 data. Left panel: fitting on $n\sigma_e$ distribution. The red curve is the electron contribution while the blue one comes from contamination. The pink curve is the overall fit function. Right panel: electron purity as a function of momentum.

For high p_T TPC+EMC electron, the purity is estimated by three gaussian fits on the $n\sigma_e$ distribution. The fitting plots can be found in Fig. 0.7. The purity can be found in Fig. 0.6. A p_T differential contribution from hadron contamination is applied to systematic uncertainty.

0.3 Pair Reconstruction

To reconstruct the invariant mass (M_{ee}) distribution, a unlike-sign method is used. With this method, two electrons with different charges are combined randomly in a same event. Eq. 0.2 is the equation of M_{ee} . These electrons pairs are called unlike-sign pairs (N_{+-}) which contain both di-electron signal and background. The signal is the di-electron generated from light flavor hadron decay, heavy flavor hadron decay, Drell-Yan and thermal radiation. Fig. 0.8 is the unlike-sign M_{ee} distribution as a function of p_T . The band

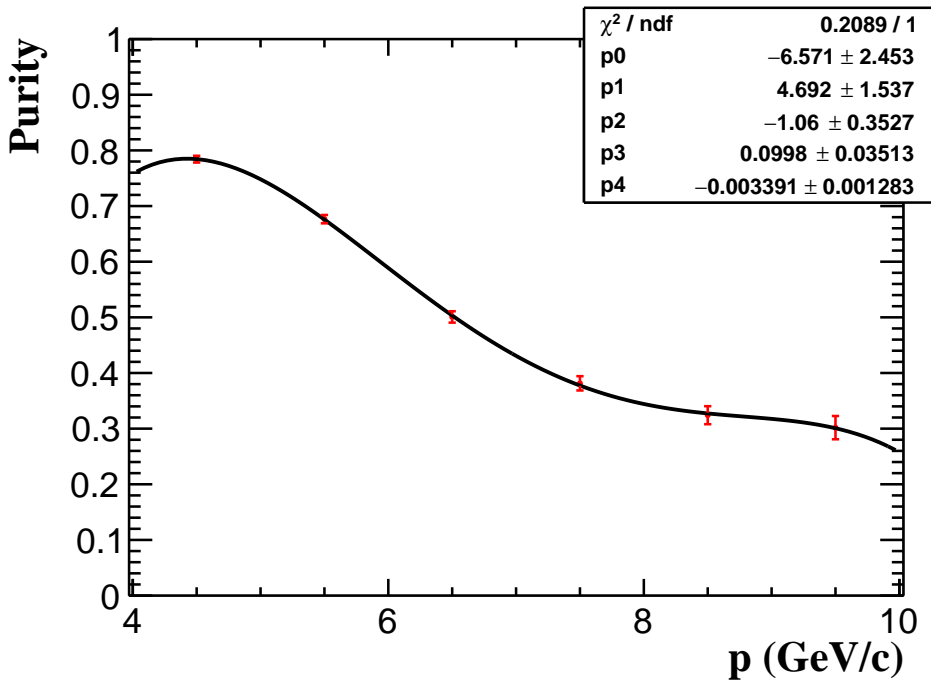


Figure 0.6: Purity for TPC+EMC electrons.

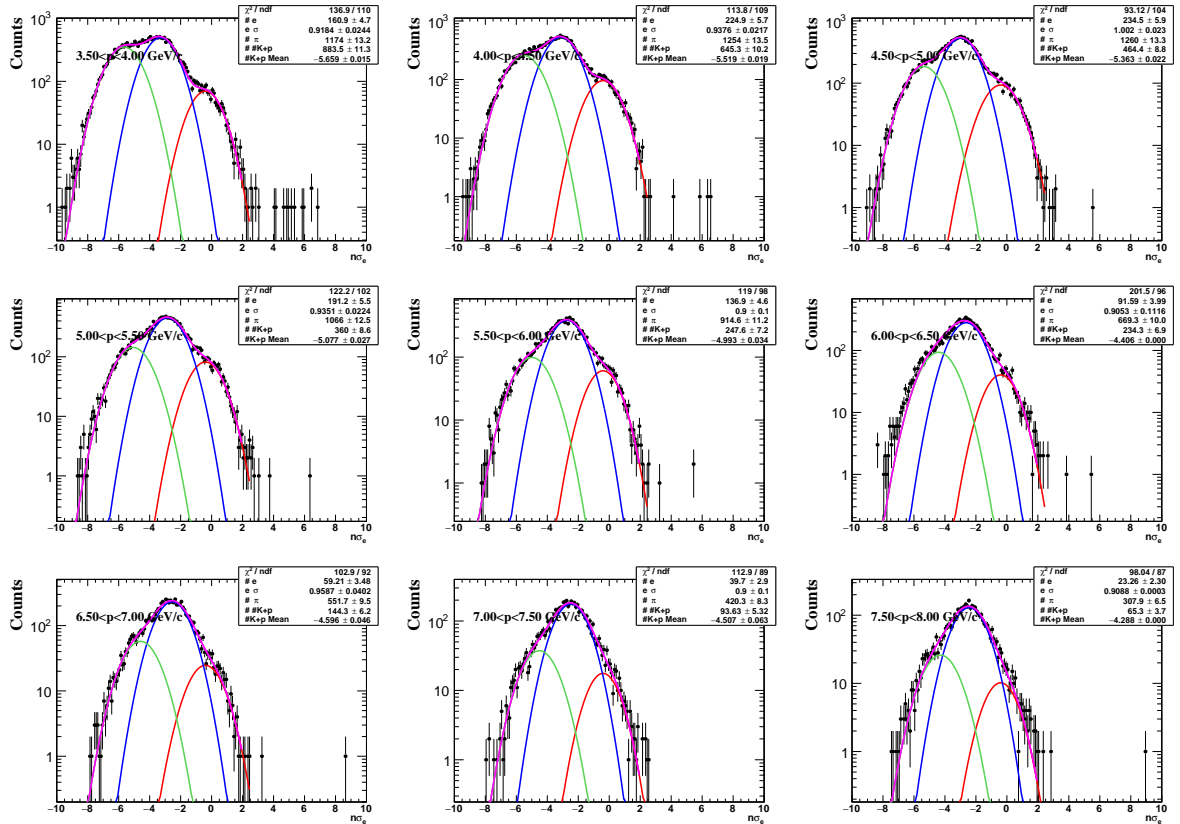


Figure 0.7: Purity fitting plots for TPC+EMC electrons in different p_T slices.

at about $3.1 \text{ GeV}/c^2$ is the signal from J/ψ . Signals from ω and ϕ which have e^+e^- decay channel is overwhelmed by the background due to the low signal/background (S/B) ratio (Fig. 0.20). The 3 bands which extend to high p_T in the very low mass region (0-0.2 GeV/c^2) are the gamma conversion contamination which will be discussed in Sec. 0.3.1.3.

$$M_{e^+e^-}^2 = (E_+ + E_-)^2 - (\vec{p}_+ + \vec{p}_-)^2 \quad (0.2)$$

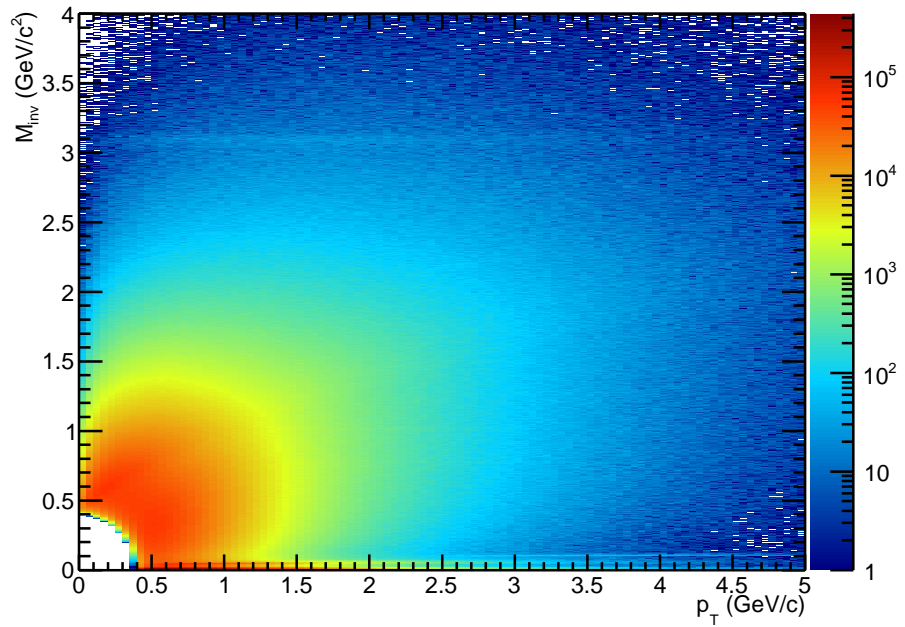


Figure 0.8: Invariant mass (M_{ee}) distribution of random combination on e^+e^- pair in same event as a function of p_T with Run11 data.

0.3.1 Background study

To get the di-electron signal, some methods for background reconstruction are studied. With the reconstructed background subtracted from unlike-sign pair, the real signal can be generated.

0.3.1.1 Like-sign method

This like-sign method is to combine the like-sign ee pair (N_{++} and N_{--}) in the same event. The only expected M_{ee} distribution difference between this like-sign ee pair and the background came from unlike-sign e^+e^- pair is the acceptance difference. This will be discussed in Sec. 0.4.3. With this acceptance difference corrected for, the signal can be generated by just subtracting the like-sign background from unlike-sign pairs. Eq. 0.3 is the formula for di-electron signal with like-sign method. $F_{acc}(M_{ee}, p_T)$ is calculated by Eq. 0.4. A geometrical mean of (N_{++} and N_{--}) is used to get the average value of like-sign pairs. In high p_T , for some bins having a zero N_{++} or N_{--} , the average of N_{++} and N_{--} is more close to the real value. Fig. 0.9 is the signal with this like-sign method. A ϕ_V cut (Sec. 0.3.1.3) is applied to reject gamma conversion background. The advantages of the like-sign method is: 1) good description on background, low residual background after background subtraction. 2) can describe correlated background. The correlated background in unlike-sign pair came from the combination of e^+e^- which are not from the same parent (not a signal) but have correlation. For example, many correlated background came from this case: one e^\pm came from π^0 Dalitz decay ($\pi^0 \rightarrow \gamma + e^+ + e^-$) and the other e^\mp came from the gamma conversion e^+e^- pair while the conversion gamma is from that Dalitz decay. This e^+e^- pair is not a signal but has correlation.

$$Signal(M_{ee}, p_T) = N_{+-}(M_{ee}, p_T) - F_{acc}(M_{ee}, p_T) \times 2\sqrt{N_{++}(M_{ee}, p_T)N_{--}(M_{ee}, p_T)} \quad (0.3)$$

0.3.1.2 Mixed-event method

The mixed-event method is another way to reconstruct the background. Different events with same or similar properties are put in the same event buffer. This method is to combine e^+e^- pair from choosing the electron candidates from different events (B_{+-}). There is absolutely no correlation between two electron candidates in a pair. The same or

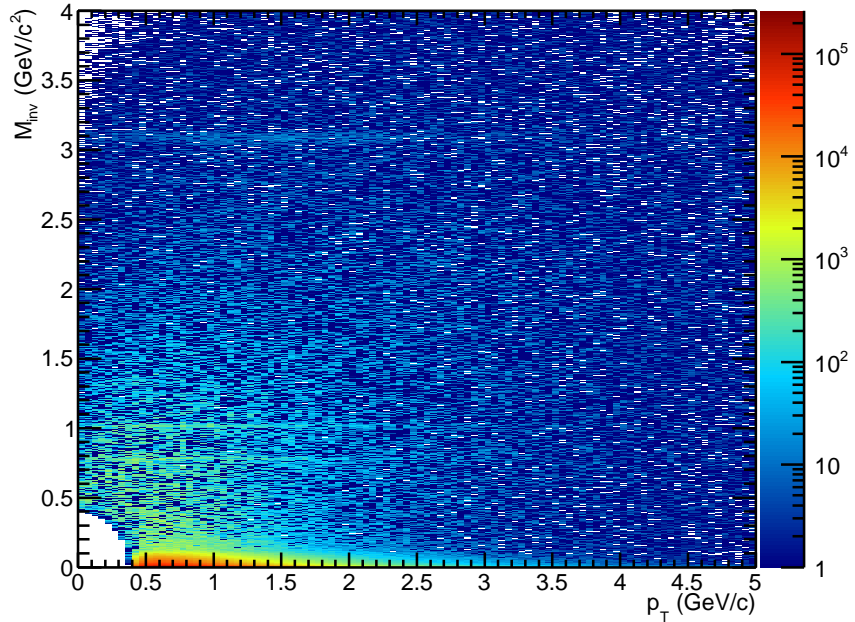


Figure 0.9: Di-electron signals (M_{ee} vs p_T) with like-sign background reconstruction method for Run11 data.

similar properties of these mixed events can make this combination describe the unlike-sign background in the same event more precisely.

In this analysis, 2 magnetic field bins, 10 vertex Z bins, 9 centrality bins, 12 event-plane bins are used to selected events for mixing. The magnetic field and vertex Z distribution can be found in Fig. 0.2. The centrality is obtained from the StRefMultCorr class. The event-plane distribution is shown in Fig. 0.10. Only the events in the same magnetic field, vz, centrality and event-plane bin can be used to mix with each other. The event pool size is set to 300 and the number of event pools is $2 \times 10 \times 9 \times 12$. 50 M events are combined together for a individual job process to make sure that the average mixed times for a event is larger than 299.

The like-sign mixed pairs (B_{++} and B_{--}) are also generated for acceptance correction purpose. The advantages of this method is: 1) low statistical errors. 2) can be used to describe the acceptance difference between unlike-sign and like-sign ee pair (Eq. 0.4, Sec. 0.4.3). But this method can not reconstruct the correlated background. Fig. 0.11 is the signal with this mixed-event method. To subtract correlated background and improve

the statistical errors, a mixture of like-sign signal and mixed-event signal is generated. The combined signal is like-sign signal ($M_{ee} < 0.7 \text{ GeV}/c^2$) plus mixed-event signal ($M_{ee} \geq 0.7 \text{ GeV}/c^2$).

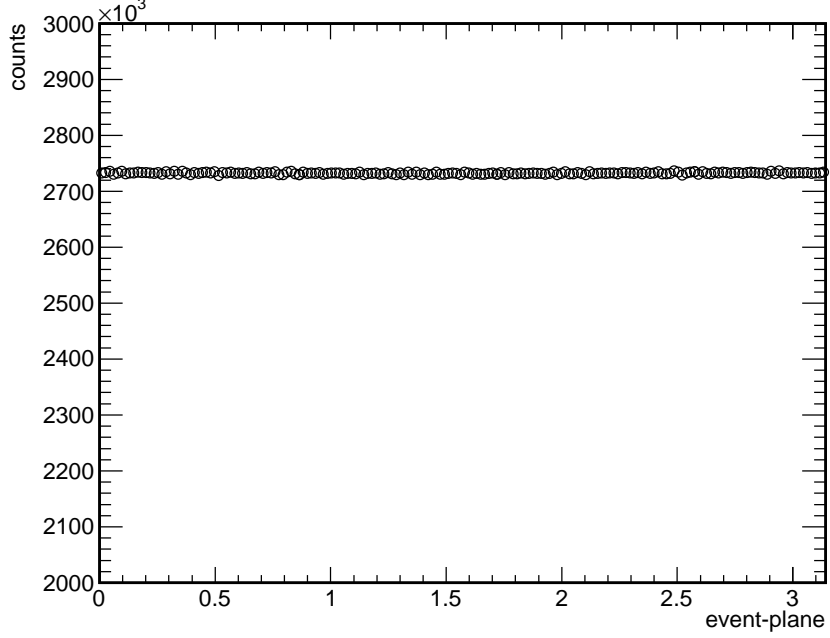


Figure 0.10: The event-plane distribution for Run11 data.

$$F_{acc}(M_{ee}, p_T) = \frac{B_{+-}(M_{ee}, p_T)}{2\sqrt{B_{++}(M_{ee}, p_T)B_{--}(M_{ee}, p_T)}} \quad (0.4)$$

0.3.1.3 Gamma conversion rejection

Some e^+e^- -pairs are from the gamma conversion caused by the interaction between γ and the detector material. These pairs need to be rejected but can not be reconstructed by neither like-sign method nor mixed-event method. The 3 bands in Fig. 0.8 which extend to high p_T in the very low mass region ($0-0.2 \text{ GeV}/c^2$) is due to this conversion process. To reject these background, a ϕ_V cut is applied. The angle ϕ_V is defined as Eq. 0.3.1.3. A diagram can be found at Fig. 0.12. The opening angle of the conversion e^+e^- pair should be very close to 0. This angle is the angle of two global tracks from a conversion vertex.

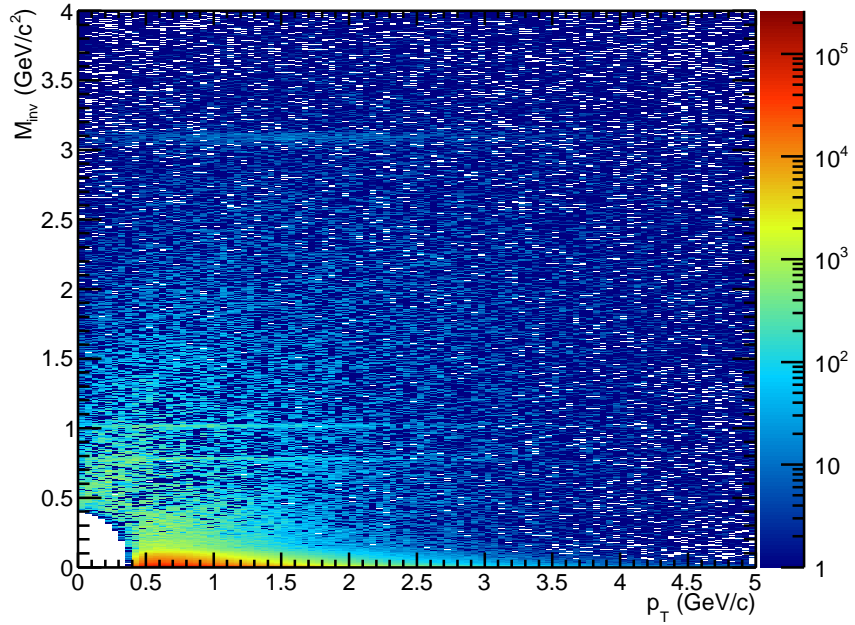


Figure 0.11: Di-electron signals (M_{ee} vs p_T) with mixed-event method with Run11 data.

After these global tracks are reconstructed to primary vertex as primary tracks, this opening angle should still be small. Fig. 0.13 is a simulation result for ϕ_V distribution of gamma conversion. There are 3 bumps from low to high mass corresponding to 3 material layers. These material layers are beam pipe ($r \sim 4cm$), inner cone supporting structure ($r \sim 20cm$) and TPC inner field cage($r \sim 46cm$). The position of these bumps are consistent with the observation from data (Fig. 0.8). The position and relative amplitude of these gamma conversion bumps have some p_T dependence. Seen from Fig. 0.13, with the increasing p_T , the “height” of third bump around $0.11\text{ GeV}/c^2$ increases and the mass shifts a little bit higher. The red line in the plot is the applied ϕ_V cut. The e^+e^- pairs with ϕ_V below the line are dropped. This cut is applied to all ee pairs of different methods. The overall gamma conversion rejection rate calculated from simulation is about 99%. From the simulated ϕ_V distribution from π^0 decayed e^+e^- pairs, the ϕ_V cut efficiency can be generated. Since there is no significant p_T dependence for π^0 decayed e^+e^- pairs’ ϕ_V distribution, the cut efficiency for all p_T range is applied to every single p_T slice when correct di-electron pair detection efficiency. Fig. 0.14 shows the ϕ_V cut efficiency and the

fit function used for efficiency correction.

$$\hat{u} = \frac{\vec{p}_+ + \vec{p}_-}{|\vec{p}_+ + \vec{p}_-|}, \quad \hat{v} = \frac{\vec{p}_+ \times \vec{p}_-}{|\vec{p}_+ \times \vec{p}_-|} \quad (0.5)$$

$$\hat{w} = \hat{u} \times \hat{v}, \quad \hat{w}_z = \hat{u} \times \hat{z} \quad (0.6)$$

$$\phi_V = \text{angle between } \hat{w} \text{ and } \hat{w}_z \quad (0.7)$$

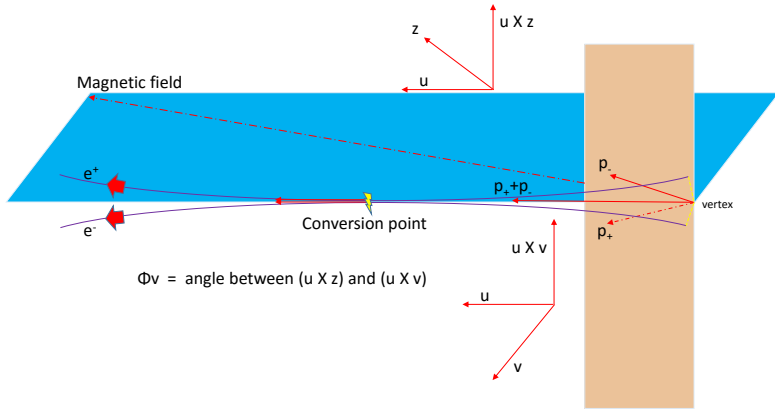


Figure 0.12: A diagram for ϕ_V definition.

Another possible way is to use global tracks to reconstruct M_{ee} . The two gamma conversion electron tracks have nearly same momentum direction at the conversion vertex. With reconstructing M_{ee} by their global momentum at the conversion vertex (the point where two global tracks are closest to each other), the 3 gamma conversion bumps should be moved to 0 GeV/c^2 . Fig. 0.15 is the distribution of M_{ee} difference between global tracks and primary tracks as a function of global mass. There are still some gamma conversion bands crossing zero with a nonzero global mass. This is caused by the worse momentum resolution of global tracks compared to primary tracks, and the reconstructed global M_{ee} can not be moved to perfect around 0 for gamma conversion e^+e^- pair. Due to this, the global mass method is not suitable to reject the gamma conversion background.

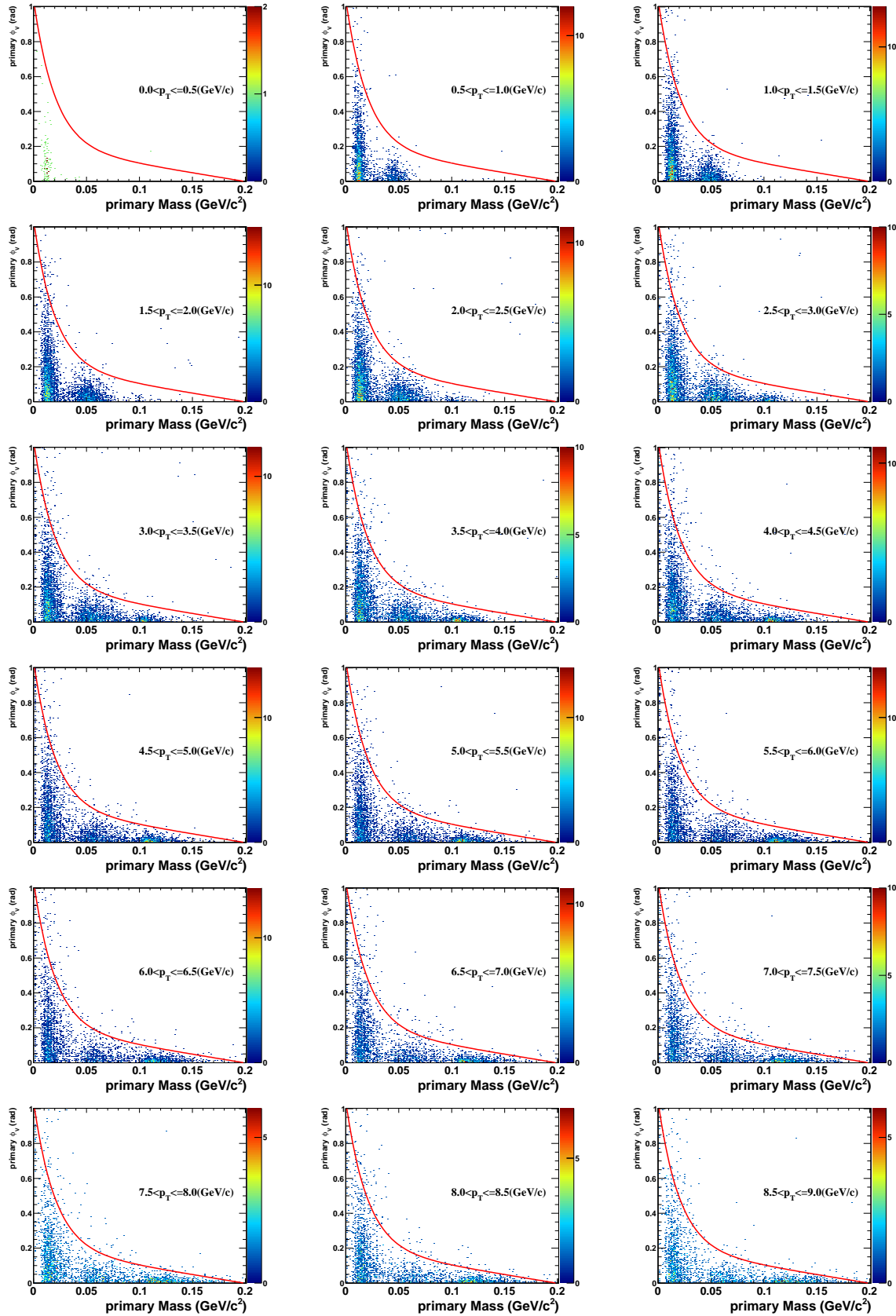


Figure 0.13: Simulation on ϕ_V distribution of gamma conversion in different p_T slices.

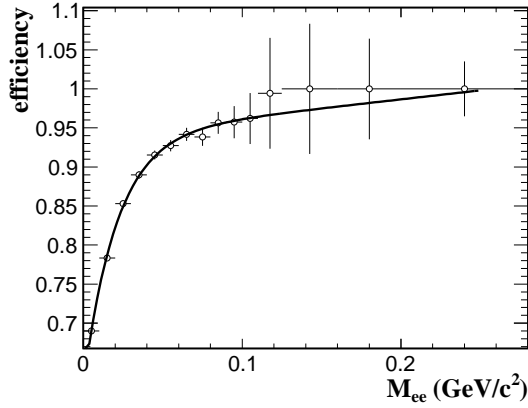


Figure 0.14: ϕ_V cut efficiency based on the pion simulation results. This efficiency is used as the ϕ_V cut efficiency on signal (after gamma rejection). The difference between virtual photon simulation and this pion simulation is taken as the systematic uncertainty from ϕ_V cut.

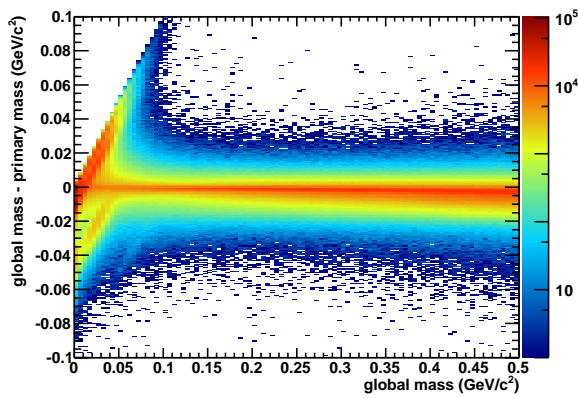


Figure 0.15: The distribution of M_{ee} difference (global mass - primary mass) as a function of global mass.

0.3.2 Raw signal

Fig. 0.16 and Fig. 0.17 shows the M_{ee} distribution for different ee pairs. The right panel is a zoom in view of different backgrounds. In the low mass region, the mixed-event background is systematically lower than the like-sign background due to the correlated background mentioned in Sec. 0.3.1.1. With the like-sign background and mixed-event background subtracted, the raw signal without efficiency correction can be generated. Fig. 0.18 and Fig. 0.19 show the raw signal with like-sign method and mixed-event method of Run10 and Run11 data, respectively. The left panels for both figures are zoom in views in low mass region without number of events and histogram bin width normalizing. The right panels are the raw signals corrected by number of events and histogram bin width. The e^+e^- pair p_T range is 0 - 10 GeV/ c for all these plots.

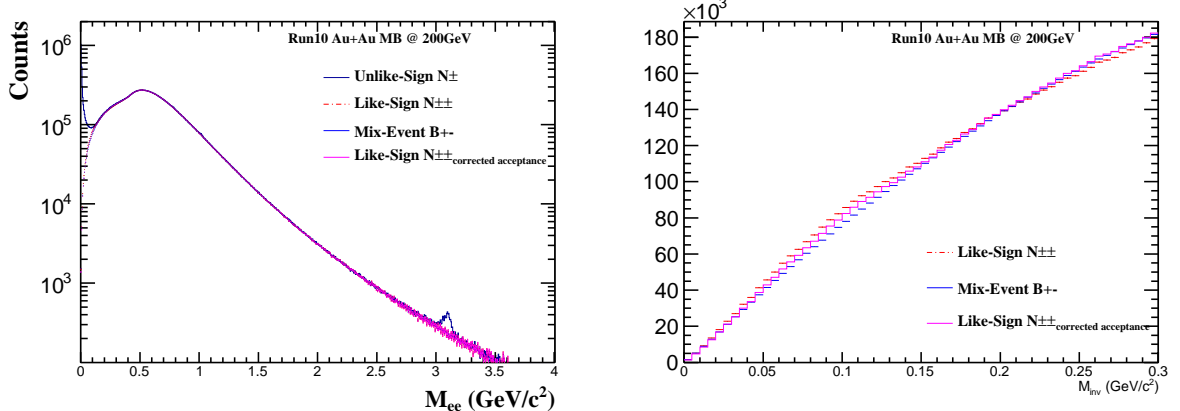


Figure 0.16: The distribution of M_{ee} with different reconstruction methods for Run10 data.

The lower mixed-event background in low mass region compared to like-sign method will give a higher raw signal. This can be seen in the left panels of Fig. 0.18 and Fig. 0.19. Fig. 0.20 shows the signal over background ratio with like-sign method.

0.4 Efficiency and Acceptance

In this analysis, the main used detectors are TPC and TOF. The TPC tracking efficiency which stands for the possibility that a real track can be reconstructed by TPC

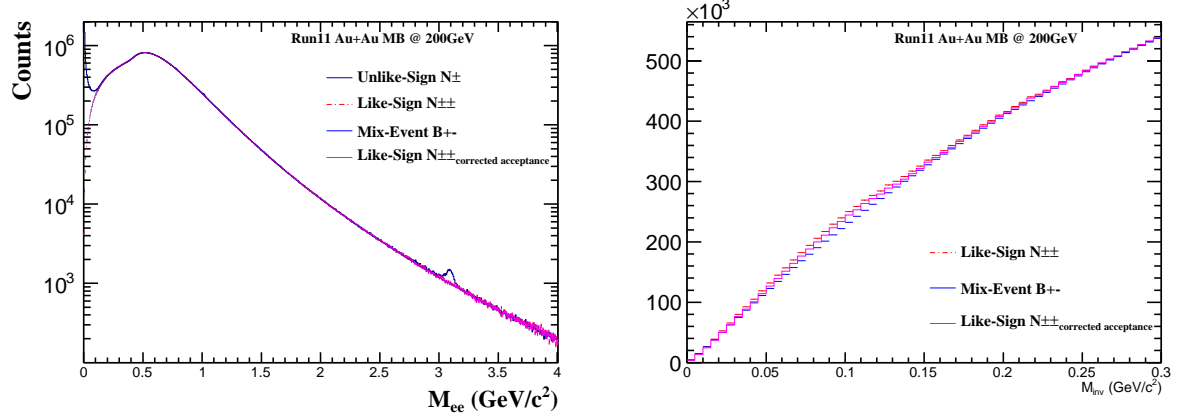


Figure 0.17: The distribution of M_{ee} with different reconstruction methods for Run11 data.

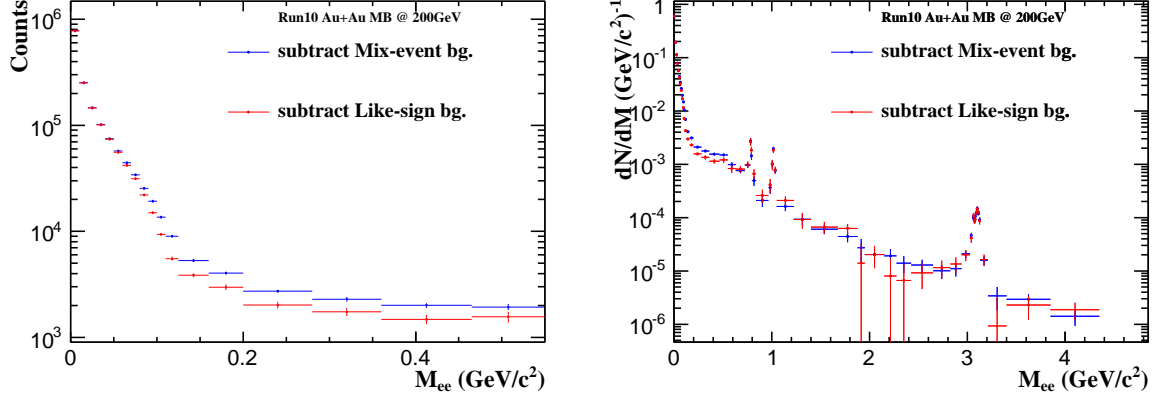


Figure 0.18: The di-electron raw signal for Run10 data. Left panel: in low mass region w/o number of events and bin width correction. Right panel: w/ number of events and bin width correction.

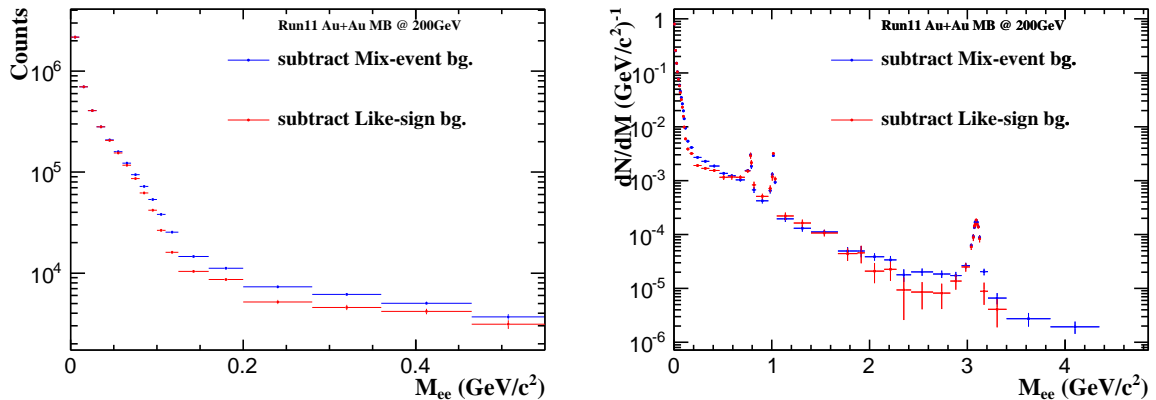


Figure 0.19: The di-electron raw signal for Run11 data. Left panel: in low mass region w/o number of events and bin width correction. Right panel: w/ number of events and bin width correction.

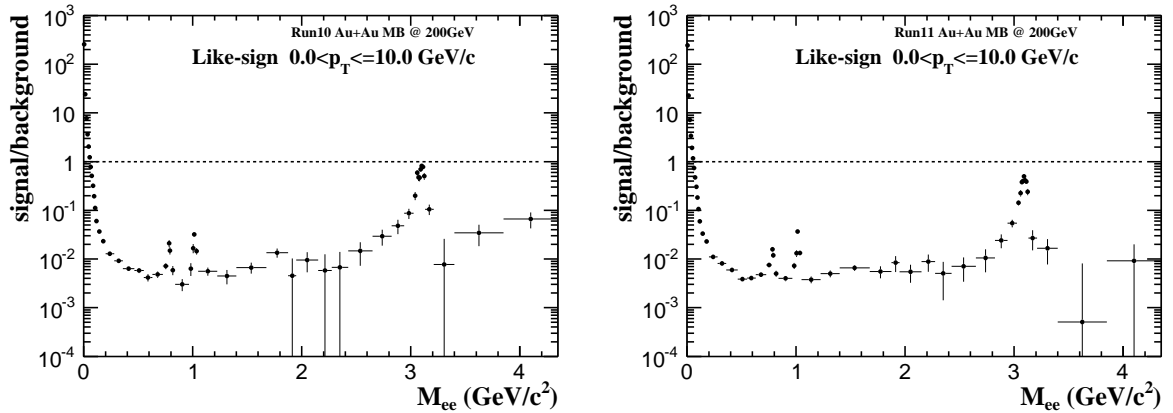


Figure 0.20: Signal over background ratio with likesign method. Left panel: Run10 data. Right panel: Run11 data.

information and TOF matching efficiency which stands for the possibility that a track passed TOF can leave a hit information will be used for efficiency correction while the acceptance caused by TPC and TOF detailed geometry should be included in. Other cut efficiencies including $n\text{HitsDedx}$ cut efficiency, $n\sigma_e$ cut efficiency and $1/\beta$ cut efficiency will be taken into account.

0.4.1 Single track efficiency

To obtain the TPC tracking efficiency, some electrons are embedded in a real event. This simulated event passes the TPC tracking reconstruction steps again to get the reconstructed information for those embedded electron tracks. With the comparison between the embedding electron and corresponding reconstructed tracks (number of reconstructed embedded tracks / number of input embedded tracks), the TPC tracking efficiency can be generated. For the acceptance of TPC have η and ϕ dependence, a three dimension (p_T , η , ϕ) efficiency is generated for further pair efficiency correction. Fig. 0.21 shows the ϕ dependence of the TPC tracking efficiency. In Run10, there is a dead T-PC sector. This can be seen clearly in these plots. The drop of the efficiency is caused by the edges and gaps of the TPC sectors. The effect of the dead sector in Run10 can be clearly seen from the upper plots. In this analysis, 20 η bins and 36 ϕ bins (12 *sectors per side* \times 3) are used to divide the TPC tracking efficiency. The efficien-

cy for *Global dca*, *nHitsFit*, *nHitsFit/nHitsMax* cuts are all included in this efficiency calculation. Fig. 0.22 is the TPC tracking efficiency as a function of p_T for Run10 and Run11.

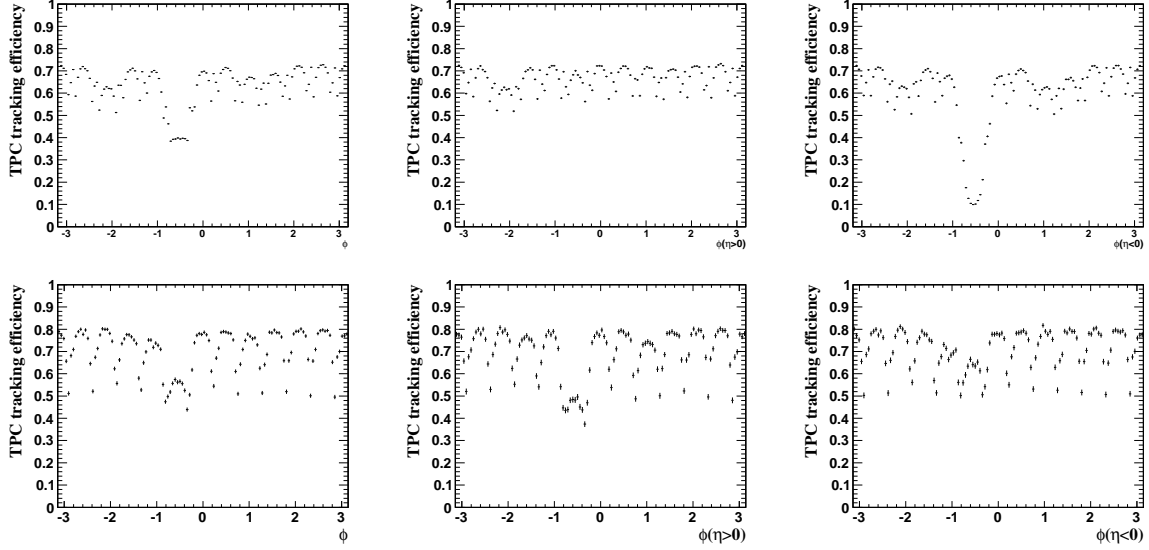


Figure 0.21: ϕ dependence of TPC tracking efficiency. Upper panels: Run10. Lower panels: Run11.

For *nHitsDedx* cut efficiency, the distribution from embedding does not describe the real data *nHitsDedx* distribution very well. So this efficiency is studied individually with the real data. The efficiency definition is shown in Eq. 0.8. Fig. 0.23 shows the *nHitsDedx* cut efficiency.

$$\varepsilon_{n\text{HitsDedx}} = \frac{N_{\text{pass other track quality cuts} + n\text{HitsDedx cut}}}{N_{\text{pass other track quality cuts}}} \quad (0.8)$$

For TOF related efficiencies, the TOF matching efficiency is defined as a ratio in which the denominator is the number of electron tracks which pass the TPC track quality cuts while the numerator is the number of electron tracks which pass the TPC track quality cuts and have TOF matching. Similar to TPC tracking efficiency, for acceptance reason, the TOF matching efficiency is divided into 20 η bins and 60 ϕ bins (*60 trays per side*). This η and ϕ dependence can be seen in Fig. 0.24. The TOF matching efficiency is calculated by using pure electron sample. The photonic electron which comes from the

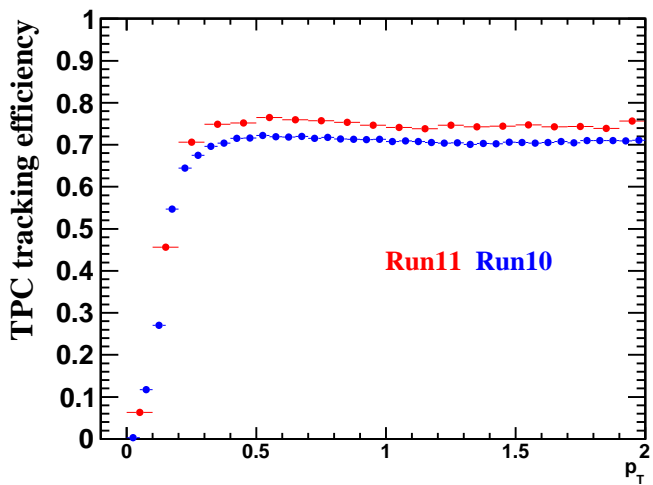


Figure 0.22: TPC tracking efficiency for Run10 and Run11. Blue: Run10. Red: Run11.

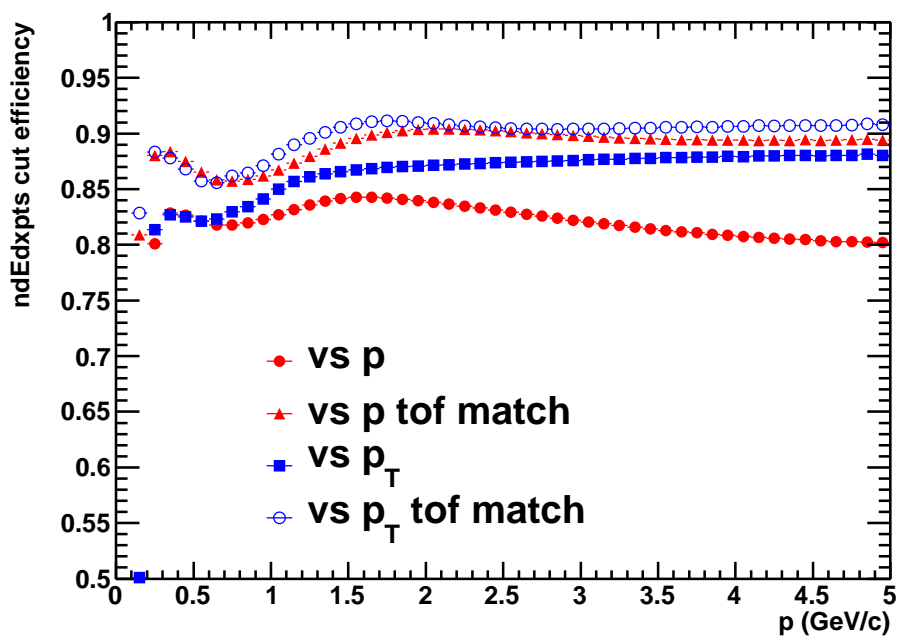


Figure 0.23: $n_{\text{Hits}}/d\text{d}x$ cut efficiency for Run11.

gamma conversion (Sec. 0.3.1.3) is chosen as this pure sample. By cutting on the opening angle of global momentum ($< 0.1\pi$), the invariant mass ($< 0.005 \text{ GeV}/c^2$) and the dca ($< 1\text{cm}$) of a e^+e^- pair, the photonic electron sample are selected. Fig. 0.25 is the TOF matching efficiencies for different particles of Run10 and Run11, respectively. Due to the limit on statistics, the efficiency of π is used as the electron efficiency by correcting the overall difference between them. This sample is also used to generate $1/\beta$ and $n\sigma$ cut efficiencies. A Gaussian fit is applied to the $1/\beta$ distribution in different momentum slices (Fig. 0.27 left panel). The $1/\beta$ cut is cutting on the difference between $1/\beta$ and these $1/\beta$ Gaussian fit mean values. Fig. 0.26 is the photonic electron $1/\beta$ distribution for Run11 data. The red markers are the Gaussian fit mean values while the red lines are the upper and lower cut edges. The blue line is the fitting results on these Gaussian fit means for Run10 data. Fig. 0.27 shows the $1/\beta$ cut efficiency for Run10 and Run11. Seen from the plots, the $1/\beta$ cut efficiency is close to 100%.

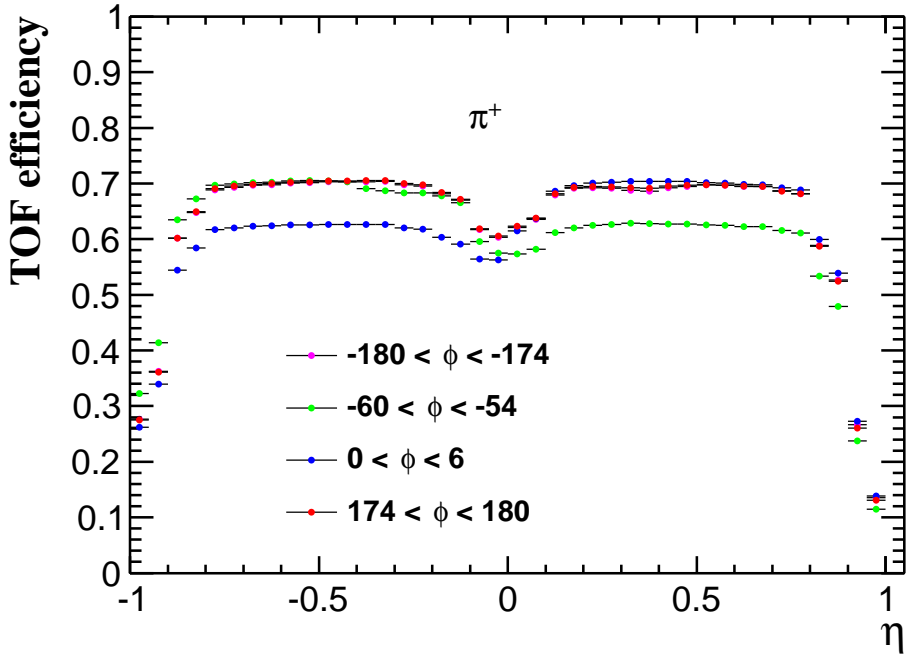


Figure 0.24: η and ϕ dependence of TOF matching efficiency for Run11 π^+

For the $n\sigma_e$ cut efficiency calculation, a Gaussian function is used to fit the electron $n\sigma_e$ distribution to constrain the electron $n\sigma_e$ distribution. By taking the ratio of the integral

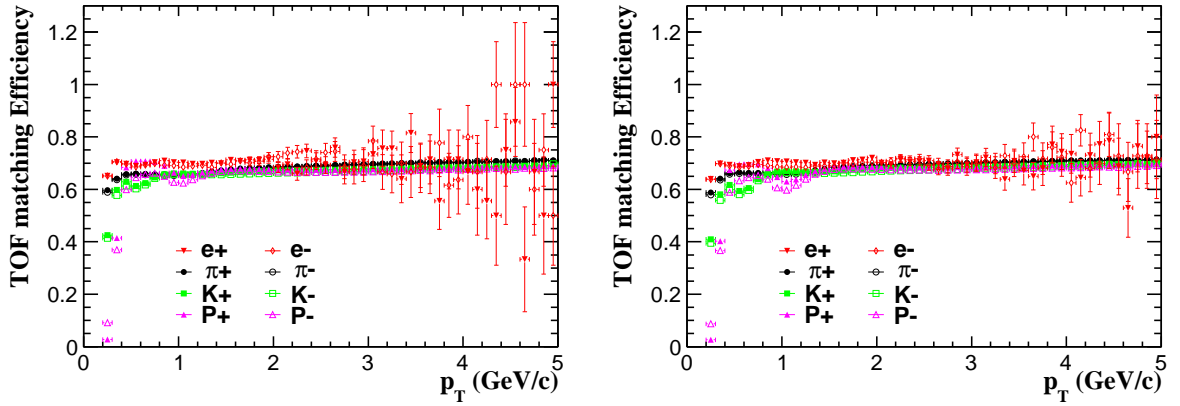


Figure 0.25: TOF matching efficiencies of different particle species for Run10 and Run11. Left panel: Run10. Right panel: Run11.

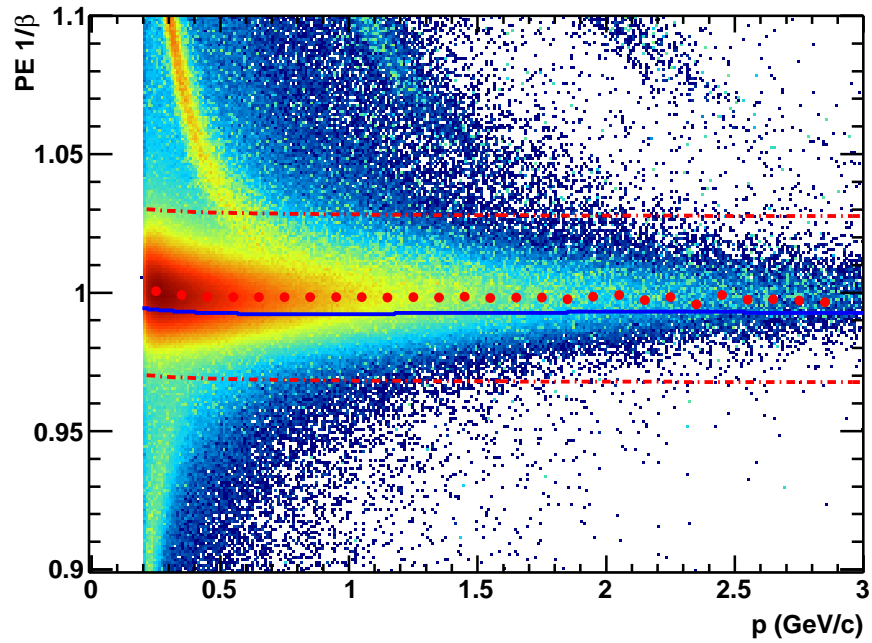


Figure 0.26: Electron $1/\beta$ distribution for Run11 data. The red lines are the upper and lower cut edges. The red markers are the Gaussian fit means in different momentum slices. The blue line is the fitting result on these fit means for Run10 data.

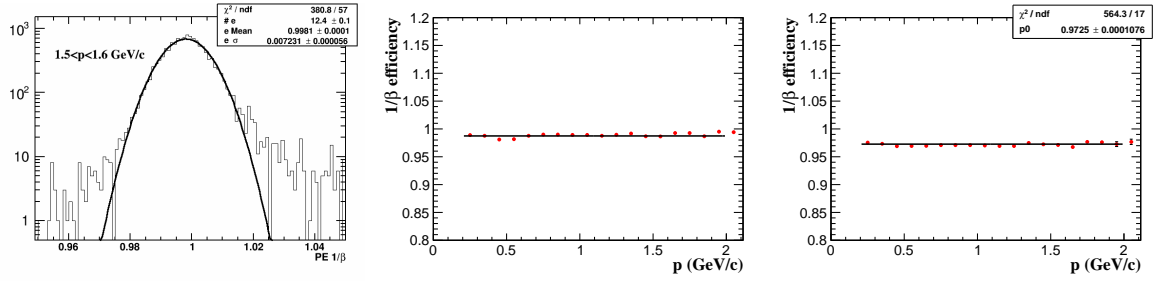


Figure 0.27: Left panel: Gaussian fit on $1/\beta$ distribution in a momentum slice for Run11. Middle panel: Run11 $1/\beta$ cut efficiency. Right panel: Run10 $1/\beta$ cut efficiency.

of this Gaussian function in cut range over the overall value, the $n\sigma_e$ cut efficiency can be obtained. Fig. 0.28 shows the $n\sigma_e$ cut efficiency based on the cut shown in Tab. 0.3. The efficiencies for two other different cuts with loose (primary lower limit - 0.2) and tight (primary lower limit + 0.2) lower cut limits are also calculated for comparison. The mean values of $n\sigma_e$ shown in the right panels explain the shift of the cuts between Run10 and Run11.

The centrality dependence single track efficiencies are generated with the exactly same procedure to those in MB data set. Only specific centrality cut is applied for specific centrality. The corresponding difference between specific centrality efficiency and MB efficiency is applied to the pair efficiency generation process in MB. The MB pair efficiency generation plus centrality dependence single track efficiency correction reconstruct the centrality dependence pair efficiency.

Fig. 0.29 shows the TPC tracking efficiency correction factors for different centralities. Fig. 0.30 shows the TOF matching efficiency correction factors for different centralities. Fig. 0.31 shows the ndEdx points efficiency correction factors for different centralities.

0.4.2 Pair efficiency

With the results of all single track efficiencies, a pair efficiency can be generated by combining the simulations of different di-electron sources. This simulation folding method is to use the decay kinematics of different di-electron sources with a flat η and ϕ input. The input p_T distribution for these sources is the measured value. The meson

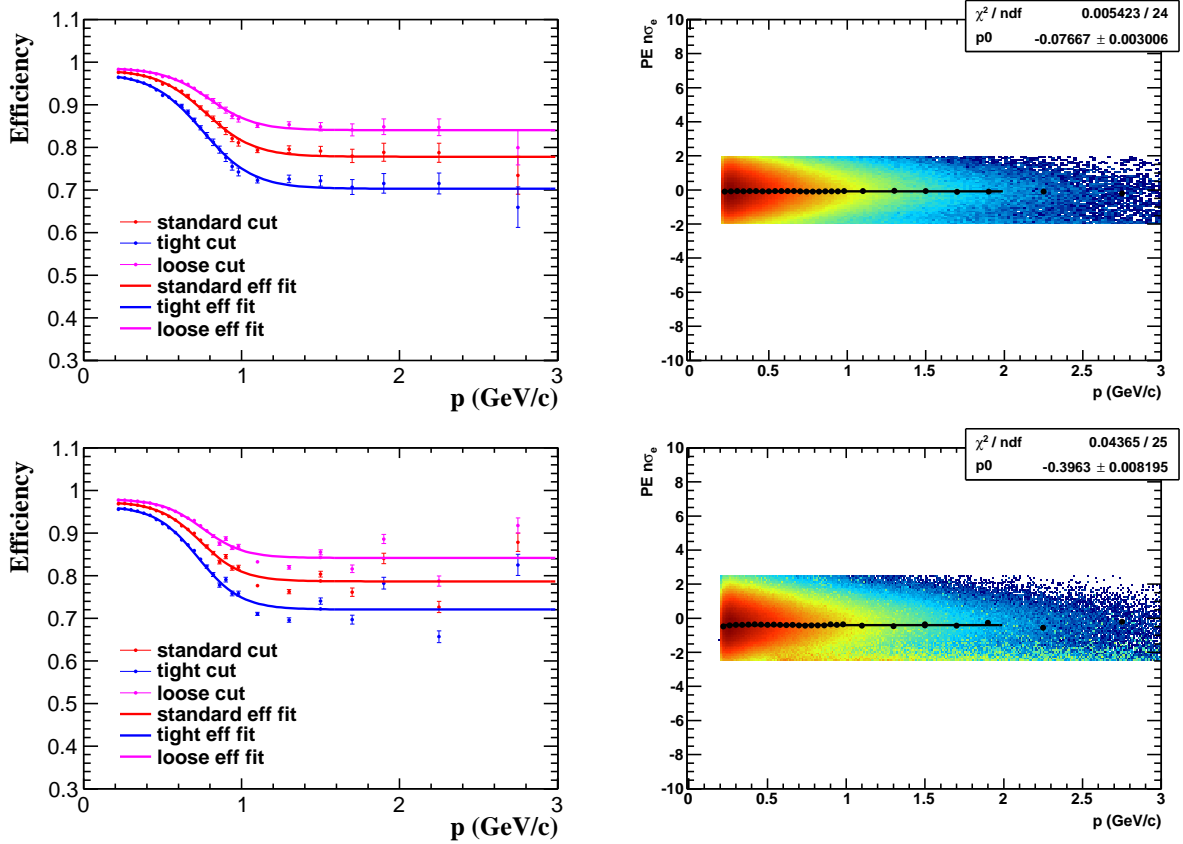


Figure 0.28: $n\sigma_e$ cut efficiencies for Run10 and Run11. Upper panels: Run10. Lower panels: Run11. Left panels: $n\sigma_e$ cut efficiency. Right panels: $n\sigma_e$ distribution of the photonic electron sample.

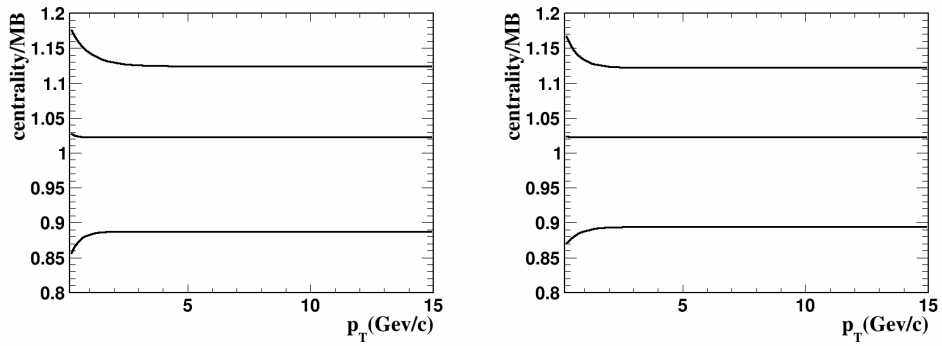


Figure 0.29: TPC tracking efficiency correction factors for different centralities. Left : Run10. Right : Run11. From upper to lower : 40-80%, 10-40%, 0-10% centralities.

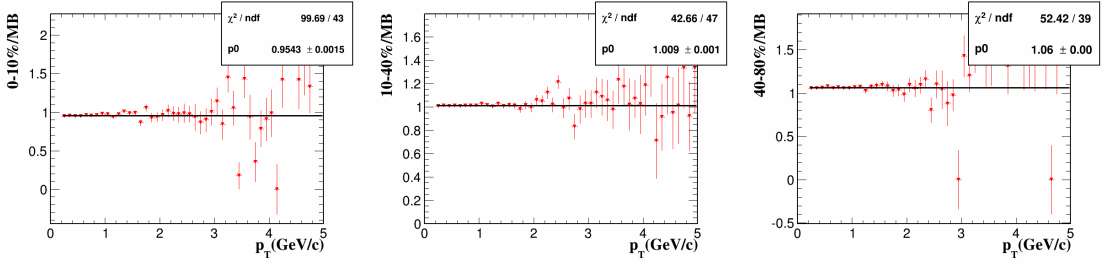


Figure 0.30: TOF matching efficiency correction factors for different centralities for Run11.

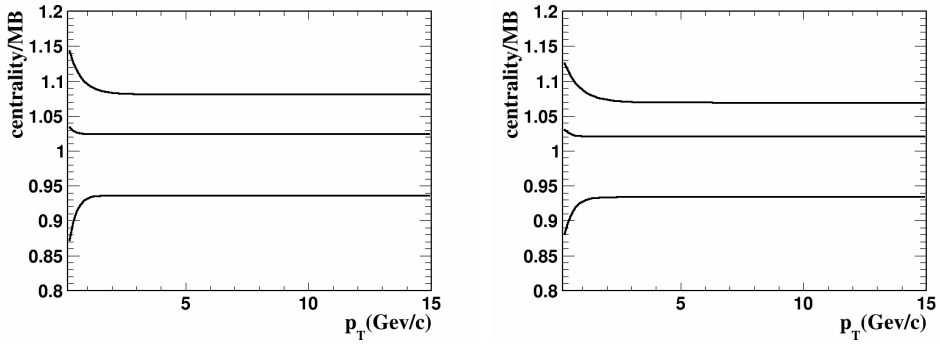


Figure 0.31: ndEdx points efficiency correction factors for different centralities. Left : Run10. Right : Run11. From upper to lower : 40-80%, 10-40%, 0-10% centralities.

momentum spectra are collected from previous publications at RHIC energy. For heavy flavor components, the non-photonic electron p_T spectra and PYTHIA were used for sampling. The details of the cocktail related simulation will be discussed in Sec. 0.5.

To get the overall single track efficiency, the product of different single track efficiencies which is generated by evaluating the specific p_T or momentum of the track is used. The product of the positron and electron overall single track efficiencies stands for the pair efficiency of this e^+e^- pair. To determine the efficiency bias caused by different kinematics, two cocktails are generated by the method shown in Sec. 0.5. One cocktail (*cocktail acc*) used as the denominator is the cocktail within the STAR acceptance ($p_T(e) > 0.2$ GeV/ c , $|y_{e^+e^-}| < 1$ and $|\eta_e| < 1$). Weighted by the positron and electron single track efficiency respectively, the cocktail (*cocktail eff*) can be generated accordingly. These cocktails can be found in Fig. 0.36. Multiplied by the ϕ_V cut efficiency, the ratio (*cocktail eff / cocktail acc*) is the pair detection efficiency within STAR acceptance. Fig. 0.32 shows the di-electron pair detection efficiency without ϕ_V cut efficiency

in different p_T slices.

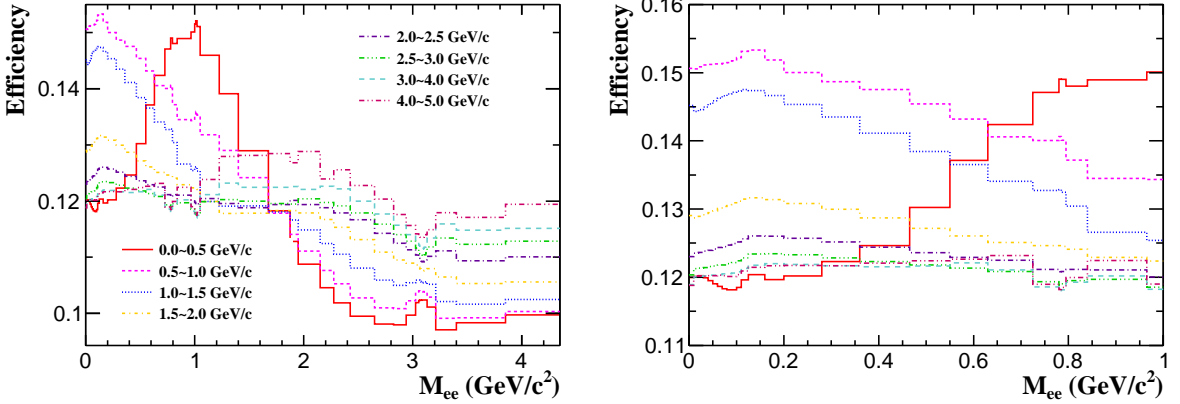


Figure 0.32: Di-electron pair detection efficiencies without ϕ_V cut efficiency in different p_T slices from Run11 Au+Au at 200 GeV.

0.4.3 Acceptance

All of the analysis results based on STAR data is within the STAR acceptance which is $p_T(e) > 0.2 \text{ GeV}/c$ and $|\eta_e| < 1$. For the di-electron measurement, the measurement is in $|y_{e^+e^-}| < 1$. $p_T(e) > 0.2 \text{ GeV}/c$ gives a low limit that the particle can pass TPC. $|\eta_e| < 1$ will make the track pass to TPC outer field cage. A simulated results which include the cocktail pass STAR acceptance (*cocktail acc*) and the cocktail without acceptance cuts (*cocktail mc*) (Fig. 0.36) can be generated to quantify this acceptance effect (*cocktail acc / cocktail mc*). Fig. 0.33 shows the STAR acceptance effect for di-electron detection.

For TPC actually does not cover the fully ϕ range, the dead area between different sectors will effect the TPC tracking efficiency. TOF also has this acceptance bias. So the efficiencies for TPC and TOF are divided into several η and ϕ bins to point this acceptance effect out. This η and ϕ dependence can be found in Fig. 0.21 and Fig. 0.24. This detailed geometry bias of TPC will also effect the acceptance difference between unlike-sign ee pair and like-sign ee pair in the magnetic field. This acceptance difference is mentioned in Sec. 0.3.1.2 and calculated by Eq. 0.4. Fig. 0.34 shows this acceptance for Run10 and Run11 calculated by Eq. 0.4. The significant difference of the two data sets

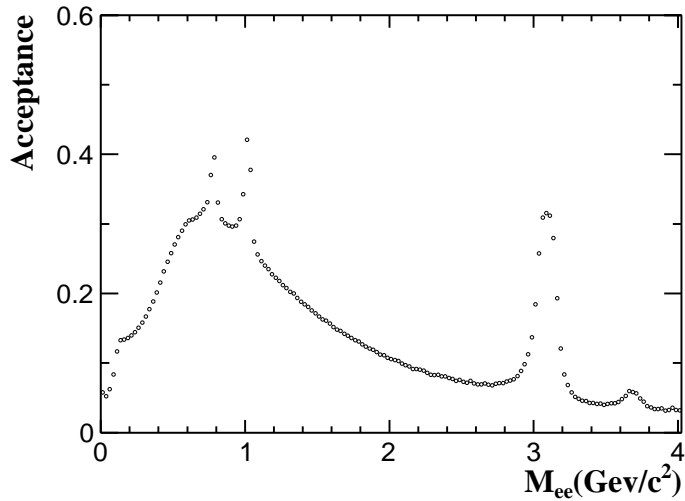


Figure 0.33: STAR acceptance in mid-rapidity for di-electron detection based on cocktail simulation (*cocktail acc / cocktail mc*).

is caused by the dead TPC sector in Run10 and gives a more profound explanation that this acceptance is caused by the TPC geometry.

In general, the STAR acceptance on di-electron detection is the acceptance of this analysis. The acceptance effects caused by TPC and TOF detailed geometry on both efficiency calculation and ee pair background reconstruction are considered and corrected.

0.5 Cocktail Simulation

The e^+e^- pairs in di-electron continuum come from the medium revolution process. The main contribution is from the decays of hadron with longer life time after the hadronic step of the medium. The combination of all of these hadron contribution is called "cocktail" which can be studied by simulation. With the comparison between the cocktail and di-electron continuum, the physics of this analysis can be studied.

0.5.1 Light flavor meson contribution

A Monte-Carlo (MC) simulation is used to study the meson contribution. The parent particles which can contribute to di-electron are generated with flat rapidity and flat

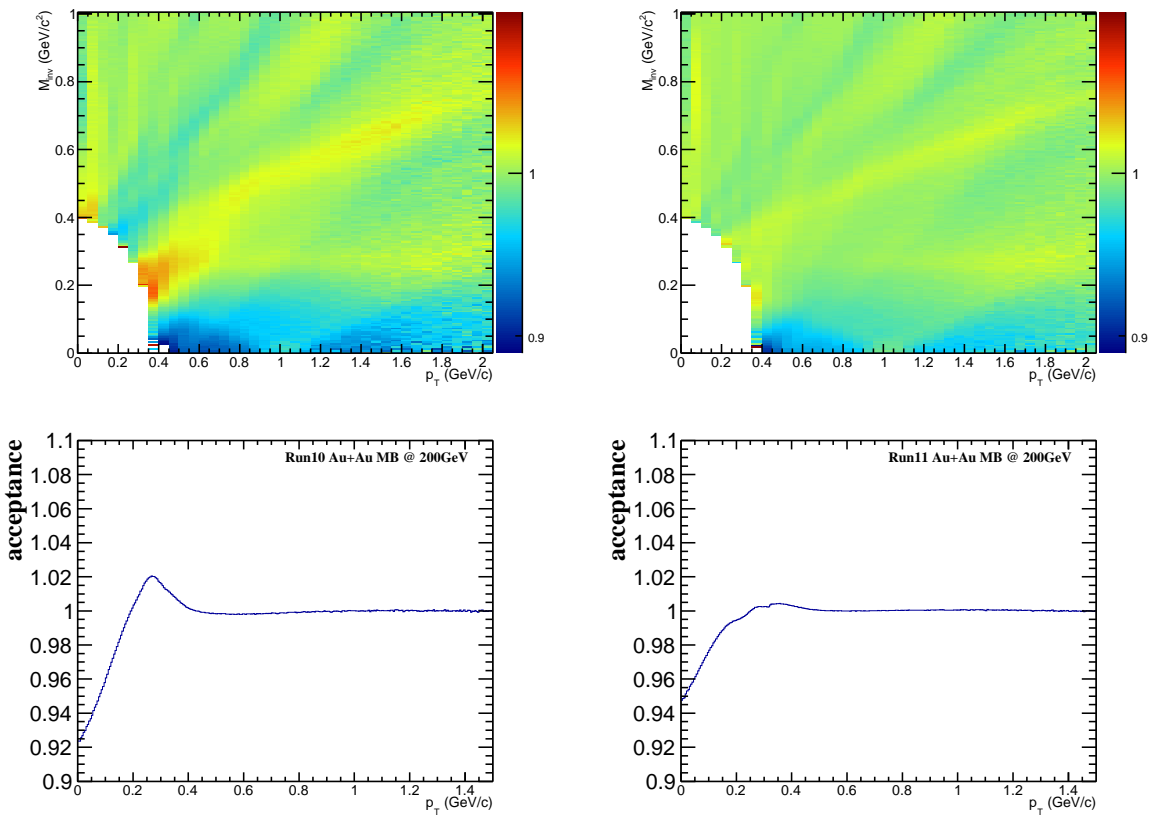


Figure 0.34: The distribution (M_{ee} vs p_T , vs p_T) of acceptance difference between unlike-sign and like-sign ee pair for Run10 and Run11. Left panels: Run10. Right panels: Run11.

azimuthal angle distribution. The input yields of these parent particles are based on a core-corona based Tsallis Blast-Wave (TBW) model fitting to the published results. The references of these published results can be found in Tab. 0.4. As shown in Fig. 0.35, the TBW model can describe the meson production in a wide p_T range. With the input p_T distribution described by the TBW model, electron pairs can be generated as the daughters after the mother particles pass the decay process with the expected dynamics. For two body decays, the mass width of the mother particles are very small compared to the mass smearing due to the detector momentum resolution. These mass widths are from PDG. For Dalitz decays, the Kroll-Wada expression is used for the $\pi^0, \eta, \eta' \rightarrow \gamma ee$, and $\omega \rightarrow \pi^0 ee, \phi \rightarrow \eta ee$ Dalitz decay calculation. In this calculation, a electromagnetic transition form factor in vacuum is considered. Eq. 0.9 shows the formula used for π^0 Dalitz decay:

$$\frac{dN}{dm_{ee}} \propto \sqrt{1 - \frac{4m_e^2}{m_{ee}^2}(1 + \frac{2m_e^2}{m_{ee}^2})} \frac{1}{m_{ee}} (1 - \frac{m_{ee}^2}{M_h^2})^3 |F(m_{ee}^2)|^2 \quad (0.9)$$

where m_e is the electron mass, m_{ee} is the e^+e^- pair mass, M_h is the mass of the hadron which decays into di-electrons. F is the electro-magnetic transition form factor.

Every meson source from a certain decay channel is weighted by its branch ratio and rapidity density (dN/dy). The sum of these meson sources is the meson contribution part in the cocktail. Adding by the contribution from heavy flavor sources, a cocktail without acceptance correction (*cocktail mc*) can be obtained. A cocktail within STAR acceptance (*cocktail acc*) which is mentioned in Sec. 0.4.3 and a cocktail weighted by efficiency (*cocktail eff*) which is mentioned in Sec. 0.4.2 can be generated accordingly. These cocktails are shown in Fig. 0.36.

Tab. 0.4 list the branch ratio and dN/dy for different meson sources. The references and uncertainties are also given in the table. The uncertainty of the dN/dy input especially for π^0 and η will affect the direct virtual photon analysis results significantly. This is considered as the systematic uncertainty and will be discussed in Sec. 0.8.

For different centralities inputs of cocktail simulation, π^0 and ϕ are with same method

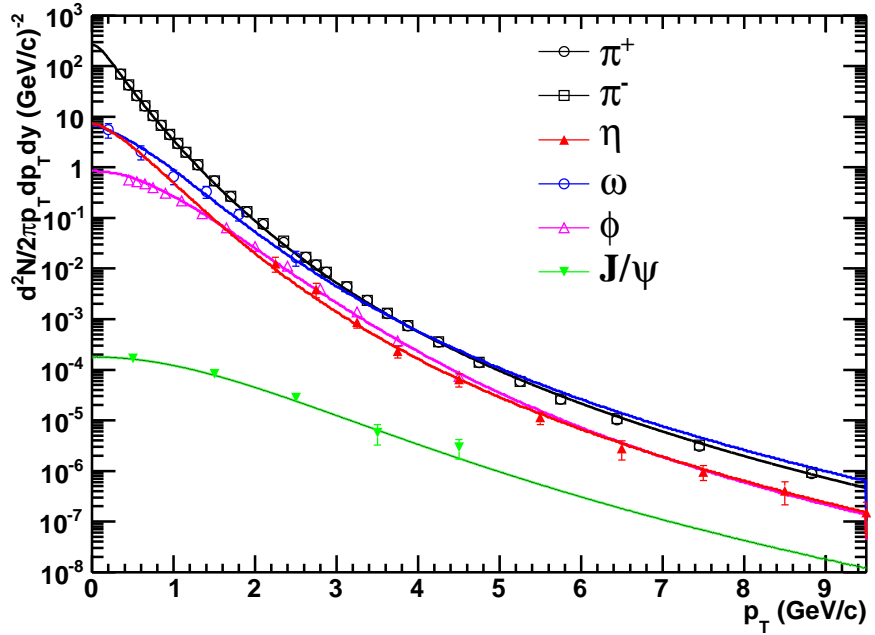


Figure 0.35: The Tsallis Blast-Wave model fitting for meson sources which are involved in cocktail simulation. The meson production are from published results in Au+Au at 200 GeV.

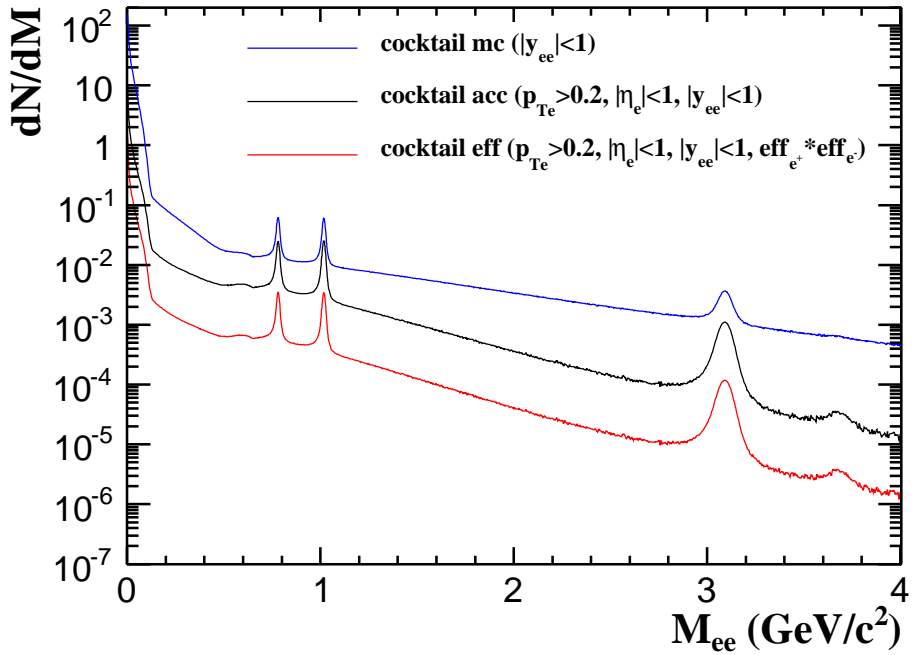


Figure 0.36: Cocktails for different acceptance settings and Run11 efficiency weighting.

Table 0.4: Branch ratio and rapidity densities (dN/dy) for different sources in the cocktail simulation.

Source	Branch ratio	dN/dy or σ	Uncertainty
$\pi^0 \rightarrow \gamma ee$	1.174×10^{-2}	98.5	8%
$\eta \rightarrow \gamma ee$	7×10^{-3}	7.86	30%
$\eta' \rightarrow \gamma ee$	4.7×10^{-4}	2.31	30%
$\omega \rightarrow \pi^0 ee$	7.7×10^{-4}	9.87	33%
$\omega \rightarrow ee$	7.28×10^{-5}		
$\phi \rightarrow \eta ee$	1.15×10^{-4}	2.43	10%
$\phi \rightarrow ee$	2.954×10^{-4}		
$J/\psi \rightarrow ee$	5.94×10^{-2}	2.33×10^{-3}	15%
$\psi' \rightarrow ee$	7.72×10^{-3}	3.38×10^{-4}	27%
$c\bar{c} \rightarrow ee$		$\sigma_{pp}^{c\bar{c}} = 0.8mb$	45
$b\bar{b} \rightarrow ee$		$\sigma_{pp}^{b\bar{b}} = 3.7\mu b$	30
$DY \rightarrow ee$	3.36×10^{-2}	$\sigma_{pp}^{c\bar{c}} = 42nb$	30%

to those in MB. TBW model is used to fit the measured data points. For other mesons, for example ω , the shape of ω is constrained by the centrality dependence TBW prediction. We scale this shape a fixed value which makes that the ω/π^0 ratio in the specific centrality is same as this in MB at 5 GeV. Fig. 0.37 shows the meson to π^0 ratio for our centrality dependence cocktail simulation inputs for different mesons in 0-10% centrality. Fig. 0.38 shows that in 10-40% while Fig. 0.39 shows that in 40-80%.

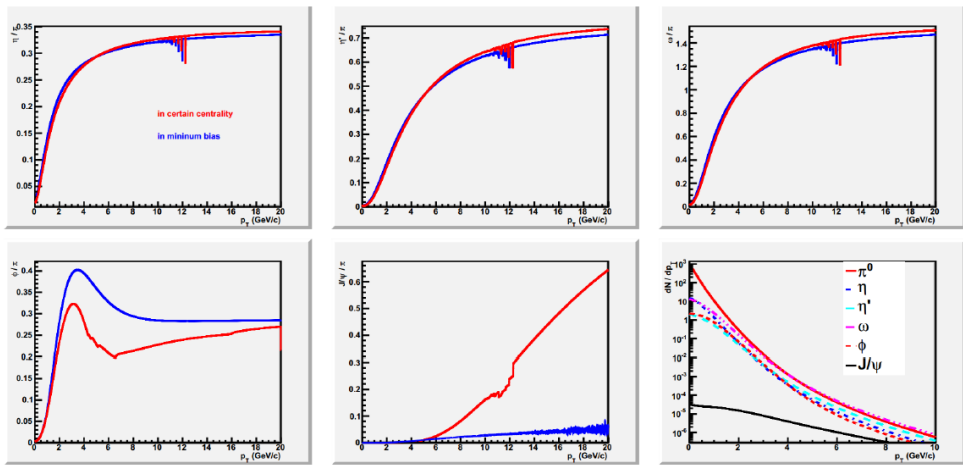


Figure 0.37: Meson to π^0 ratio for our centrality dependence cocktail simulation inputs for different mesons in 0-10% centrality

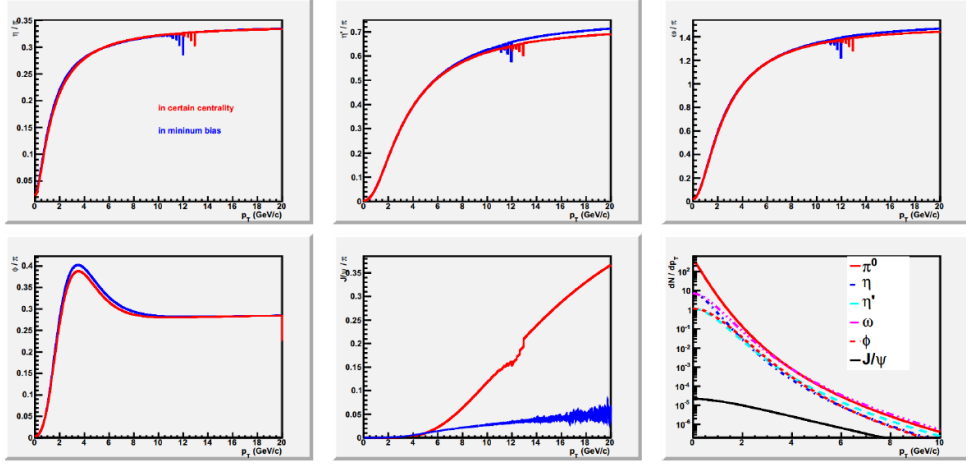


Figure 0.38: Meson to π^0 ratio for our centrality dependence cocktail simulation inputs for different mesons in 10-40% centrality

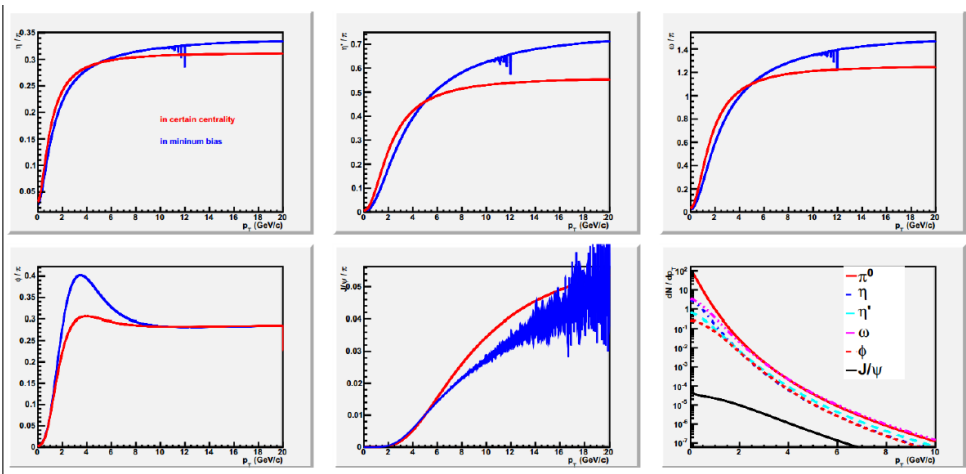


Figure 0.39: Meson to π^0 ratio for our centrality dependence cocktail simulation inputs for different mesons in 40-80% centrality

Fig. 0.40 shows the input dN/dy for different centralities. "Integral" means the dN/dy is generated by the direct integral of the p_T spectra in particular centrality. "Scale" means the dN/dy is generated by scaling the dN/dy for that meson in MB a fixed value which is the ratio of π^0 dN/dy in that centrality to MB. For example, $dN/dy_\omega = dN/dy_\omega^{MB} \times dN/dy_{\pi^0}/dN/dy_{\pi^0}^{MB}$. In the cocktail simulation, the "Scale" ones are applied.

		Pi0	Eta	etaPrim	omega	phi
0-10%	Integral	288	17.2	4.99	24.1	6.97
	scale		23.0	6.75	28.8	
10-40%		135	8.94	2.82	13.2	3.48
			10.8	3.17	13.5	
40-80%		31.4	2.55	1.07	4.41	0.682
			2.50	0.736	3.14	

Figure 0.40: dN/dy input for cocktail simulation

0.5.2 Heavy flavor contribution

For heavy flavor source, PYTHIA is used as the generator to calculate these processes in $p + p$ collisions. The cross sections and branch ratios of these heavy flavor sources are listed in Tab. 0.4. For charm contribution, the branch ratios are considered respectively according to the mother particles (D mesons) of the final e^+e^- pair in PYTHIA simulation. For bottom contribution, these branch ratios are also applied individually based on the final e^+e^- pairs' mother particles (B mesons). In Au+Au collisions, these cross sections follow the number of binary (N_{bin}) scaling, so the cross sections from $p + p$ are scaled by the number of binary collisions for MB data to match with data. Fig. 0.41 shows the cocktail within STAR acceptance in Au+Au at 200GeV and different contributed sources are shown in the same plot.

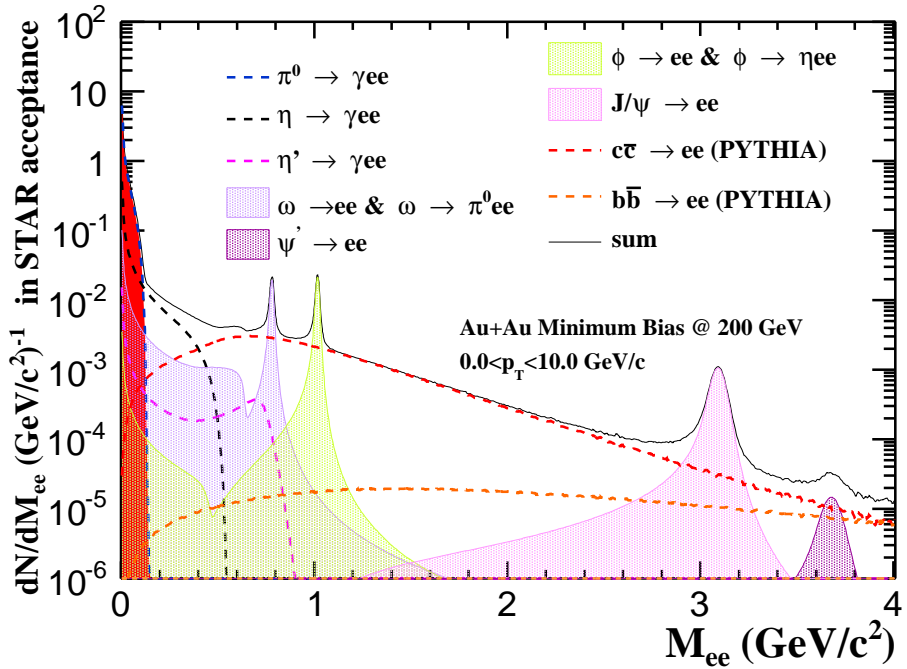


Figure 0.41: The cocktail within STAR acceptance in Au+Au at 200GeV.

0.6 Di-electron Signal

Corrected by the pair detection efficiency, the di-electron signal can be generated from the raw signal. Fig. 0.42 shows the efficiency corrected di-electron signals for Run10 and Run11 with statistical errors only. To combine the Run10 and Run11 di-electron continuum, they are treated as unequal precision measurements and are combined by their relative statistical errors bin by bin. The combined di-electron continuum can be found in Fig. 0.43 in different p_T slices for different centralities. For $p_T < 5\text{GeV}/c$, the results are from MB trigger. For p_T above $5\text{GeV}/c$, the results are from NPE18 trigger only from Run11. This high p_T extension is discussed in Sec. 0.6.1. The systematic uncertainties are discussed in Sec. 0.8. Fig. 0.44 show the difference between Run10 and Run11 signals as a function of p_T in different centralities with the combined signals as reference. Seen from plots, in the region with good statistics, the difference between Run10 and Run11 signals is lower than 5%.

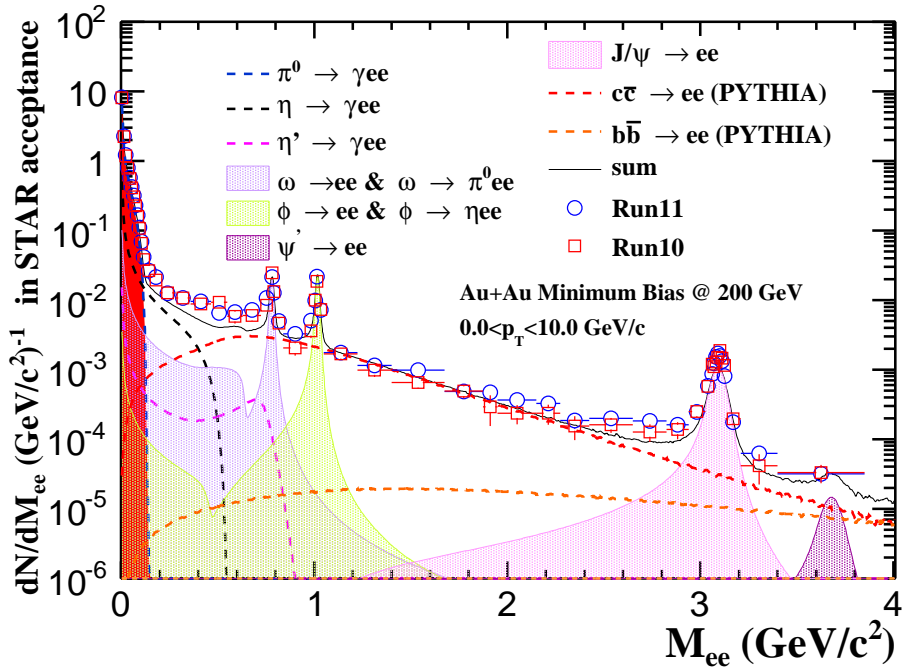


Figure 0.42: The di-electron continuum from Run10 and Run11 compared to cocktail with different contributions.

0.6.1 Di-electron continuum in high p_T

The statistics for Run10 and Run11 MB data is not enough for the high p_T study. To extend this analysis to high p_T , the BEMC triggered events are used. The track quality cuts are listed in Tab. 0.5. A “TPC + TOF” track and a “TPC + EMC” track are combined as a pair which includes at least an electron track with high p_T . The data are from Run11 200GeV “NPE18” (energy threshold 4.3GeV) triggered events. The total events number is 101.16M. 38.7M out of 88.5M pass the event selection cuts after reject bad runs. This number is equal to 6537M MB data.

The efficiency for single electron which is selected by TPC+EMC is shown in the left panel in Fig. 0.45 while the right panel shows the pair detection efficiency. A efficiency corrected di-electron continuum in 4-10 GeV/ c can be found in Fig. 0.43.

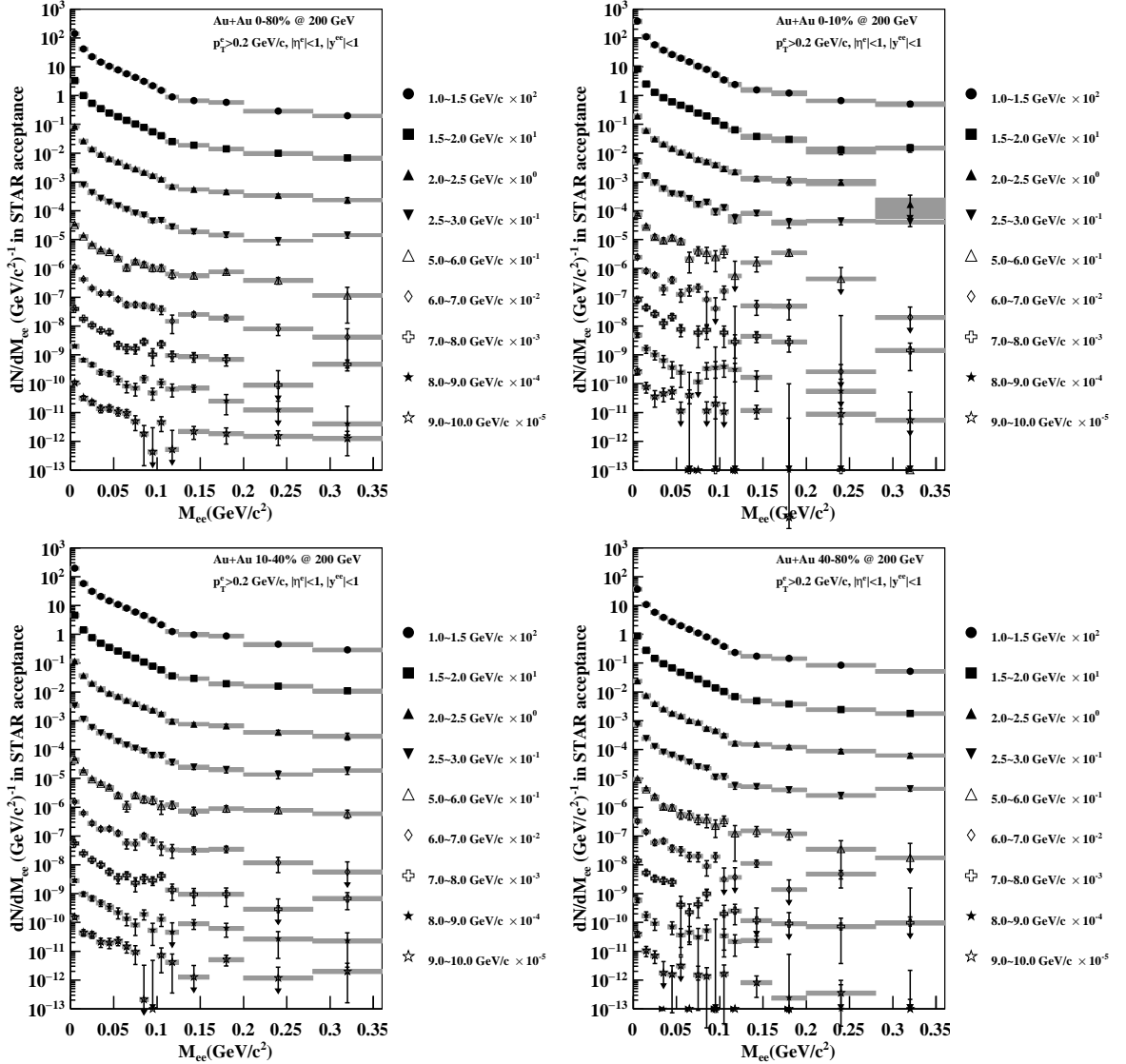


Figure 0.43: The combined di-electron continuum of Run10 and Run11 as a function of p_T in different centralities. Upper left : 0-80%. Upper right : 0-10%. Lower left : 10-40%. Lower right : 40-80%.

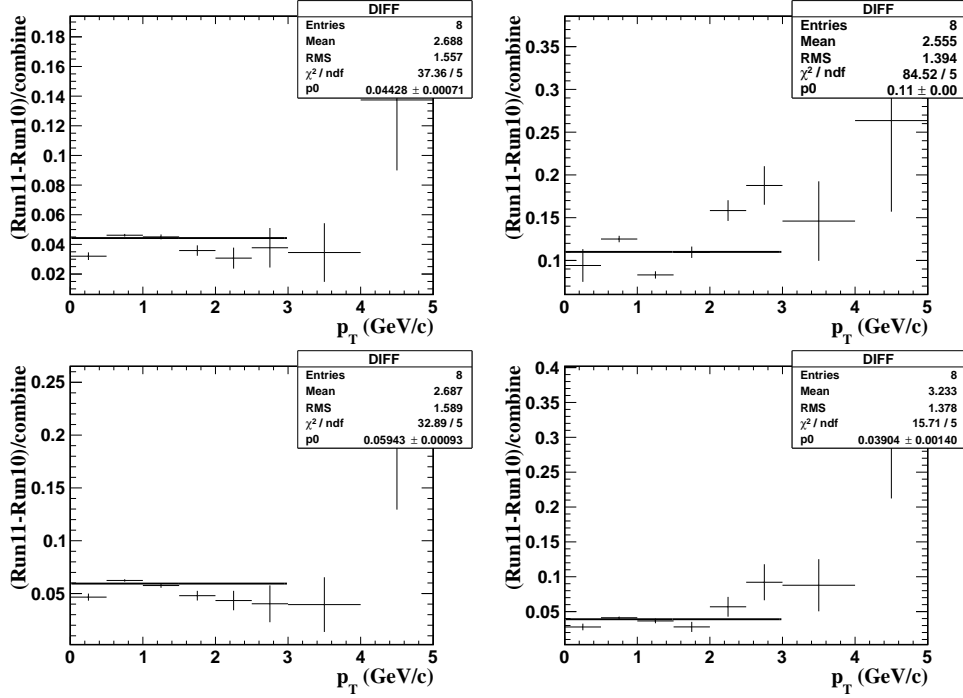


Figure 0.44: The difference between Run10 and Run11 signals as a function of p_T in different centralities. Upper left : 0-80%. Upper right : 0-10%. Lower left : 10-40%. Lower right : 40-80%.

Table 0.5: Track quality cuts for EMC triggered data.

Item	TPC+TOF track cut	TPC+EMC track cut
p_T	$0.2 < p_T < 30\text{GeV}/c$	$p_T > 3.5\text{GeV}/c$
p	$0.2 < p < 30\text{GeV}/c$	
$ \eta $	< 1	< 1
<i>Global dca</i>	$< 1\text{cm}$	$< 1\text{cm}$
$n\text{HitsFit}$	≥ 25	≥ 25
$n\text{HitsDedx}$	≥ 15	≥ 15
$PairY$	≤ 1	≤ 1
$ 1/\beta - 1 $	≤ 0.03	
$n\sigma_e$	$\leq 1.6 \& \& \geq -2.7 + 1.5p$	$\leq 1.6 \& \& \geq -1.2$
p/E		$\geq 0.3 \& \& \leq 1.5$
$adc0$		> 300

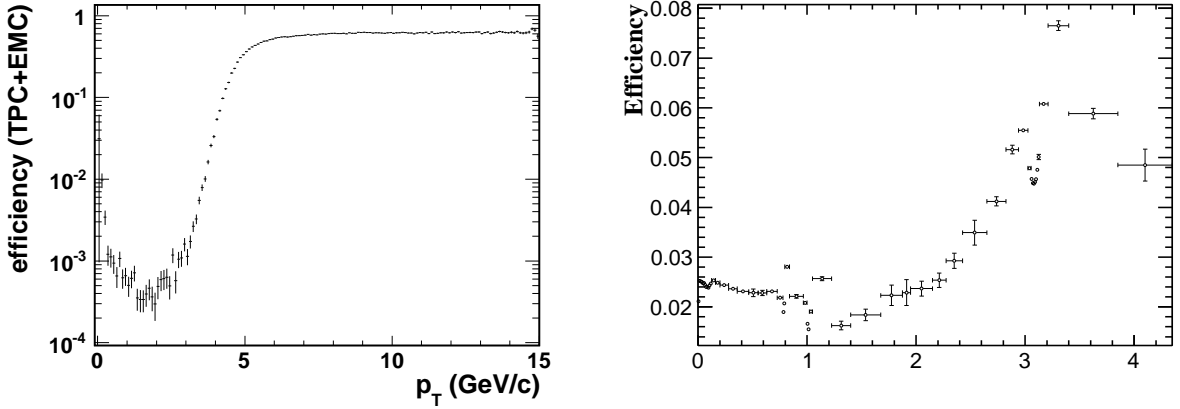


Figure 0.45: Left panel: Single electron efficiency TPC+EMC. Right panel: Pair detection efficiency in high p_T range (5-10 GeV/c).

0.7 Direct Virtual Photon Production

The behavior of low-mass excess ($M_{ee} < 0.28$ GeV/c) of di-electron continuum in Au+Au collisions is shown in Fig. 0.43. A contribution from internal conversion of direct virtual photons is expected. In general, any source of high energy photons will emit virtual photons which convert to low-mass e^+e^- pairs. A process which generated a high energy photon ($Q^2 = 0$) also have a analogous process with a virtual photon ($Q^2 = m_{\gamma^*}$). If $m_{\gamma^*} > 2m_e$, this virtual photon will materialize into e^+e^- pair. This e^+e^- pair production process is a QED correction to the real photon production process and is called internal conversion. In this analysis, the measurement of low-mass di-electron continuum is used to deduce the production of direct virtual photons.

0.7.1 Direct virtual photon and the associated e^+e^- pairs

The relation between virtual photon and the associated e^+e^- pair production can be described as Eq. 0.10.

$$\frac{d^2N_{ee}}{dM^2} = \frac{\alpha}{3\pi} \frac{L(M)}{M^2} dN_{\gamma^*} \quad (0.10)$$

$$L(M) = \sqrt{1 - \frac{4m_e^2}{M^2}(1 + \frac{2m_e^2}{M^2})} \quad (0.11)$$

In Eq. 0.10, M is the mass of the virtual photon or the e^+e^- pair mass ($M = m_{\gamma^*} = M_{ee}$). α is the fine structure constant ($\simeq 1/137$). This equation is the QED description on virtual photon to e^+e^- pair process based on the first order calculation in the electromagnetic coupling α . It is very similar to Eq. 0.9 as $M_h = m_{ee}$. If a factor $S(M,q)$ can describe the difference between real photon process and virtual photon process, Eq. 0.10 can be written as Eq. 0.12. q is the three-momentum of the virtual photon. $S(M,q)$ is a process dependent factor and be affected by such as form factors, phase space and spectral functions. As $M \rightarrow 0, q \gg M$, $S(M,q)$ is very close to unity. In this analysis, this factor $S(M,q)$ is assumed to 1 in the range $M_{ee} < 0.28 \text{ GeV}/c^2, p_T > 1 \text{ GeV}/c$. The direct virtual photon based on this assumption is called direct virtual photon. With this assumption, Eq. 0.12 can be written as Eq. 0.13. Based on this relationship, the measurement of di-electron continuum in low-mass region will deduce the production of the direct virtual photon.

$$\frac{d^2N_{ee}}{dM^2} = \frac{\alpha}{3\pi} \frac{L(M)}{M^2} S(M, q) dN_\gamma \quad (0.12)$$

$$\frac{d^2N_{ee}}{dM} = \frac{2\alpha}{3\pi} \frac{L(M)}{M} dN_\gamma \quad (0.13)$$

0.7.2 Excess in low-mass region

Fig. 0.43 shows the di-electron continuum compared to cocktail (Sec. 0.5) in p_T slices. The behavior of the excess is consistent with the expected contribution of the internal conversion of virtual photon. In this range, $M_{ee} \gg m_e, p_T \gg M_{ee}$ and $L(M_{ee}) \approx 1$. From Eq. 0.13, if there is real direct virtual photon production in a given p_T bin, the corresponding e^+e^- pairs' mass distribution will follow a $1/M_{ee}$ shape in the same p_T bin. This allows the measurement on this real direct virtual photon production via the yield

of the excess.

0.7.3 Fraction of the direct virtual photon

A limit of this study is set to $0.1 < M_{ee} < 0.28 \text{ GeV}/c^2$, $p_T > 1 \text{ GeV}/c$ to meet the requirements:

1. $p_T \gg M_{ee}$ for the lowest p_T bin $1 \sim 1.5 \text{ GeV}/c$
2. minimize the contribution from $c\bar{c} \rightarrow ee$
3. making $S(M, q)$ very close to unity
4. corresponding to the π^0 Dalitz decay cutoff caused by the decay kinematic

A two-components fitting is applied to this mass region. One component is the hadron cocktail came from simulation while the other is the $1/M_{ee}$ like function which stands for the contribution from internal conversion. The total function is written as Eq. 0.14.

$$f(M_{ee}, r) = (1 - r)f_c(M_{ee}) + rf_{dir}(M_{ee}) \quad (0.14)$$

In this equation, r is the fraction of the direct virtual photon and stands for the ratio of *direct virtual photon / inclusive photon*. $f_c(M_{ee})$ is the cocktail shown in Fig. 0.43 normalized to very low mass region ($M_{ee} < 0.03 \text{ GeV}/c^2$). And $f_{dir}(M_{ee})$ is the expected $1/M_{ee}$ like shape corresponding to internal conversion filtered through STAR acceptance and normalized to the same mass region. In this mass region, $S(M_{ee})$ (corresponding to the form factor in Eq. 0.9) of π^0 Dalitz decays which is the dominate source in the cocktail is very close to 1. Thus the functional shapes of $f_c(M_{ee})$ and $f_{dir}(M_{ee})$ are essentially identical and equal to $L(M_{ee})/M_{ee}$ smeared by the detector effects. The fitting function (Eq. 0.14) in this range is independent to the only parameter r . The STAR acceptance for e^+e^- pair correspond to internal conversion is generated as a similar method discussed in Sec. 0.4.3 with PHENIX published direct virtual photon p_T shape as an input. Fig. 0.46 shows the $L(M_{ee})/M_{ee}$ shapes smeared by the STAR acceptance for virtual photon decayed e^+e^- pair in different p_T slices. The p_T dependence is obvious in low p_T range. With

this acceptance correction and the normalization to $M_{ee} < 0.03 \text{ GeV}/c^2$, $f_{dir}(M_{ee})$ can be written as Eq. 0.15. F is the normalization factor.

$$f_{dir}(M_{ee}) = F * \left(\frac{L(M_{ee})}{M_{ee}} \right) |_{STAR\text{acceptance}} \quad (0.15)$$

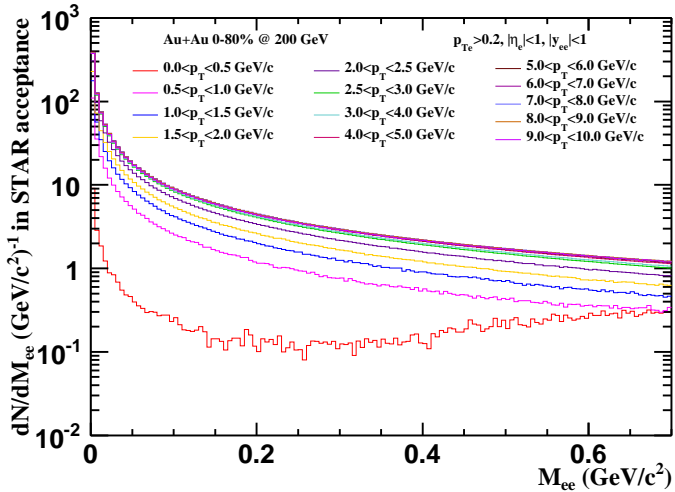
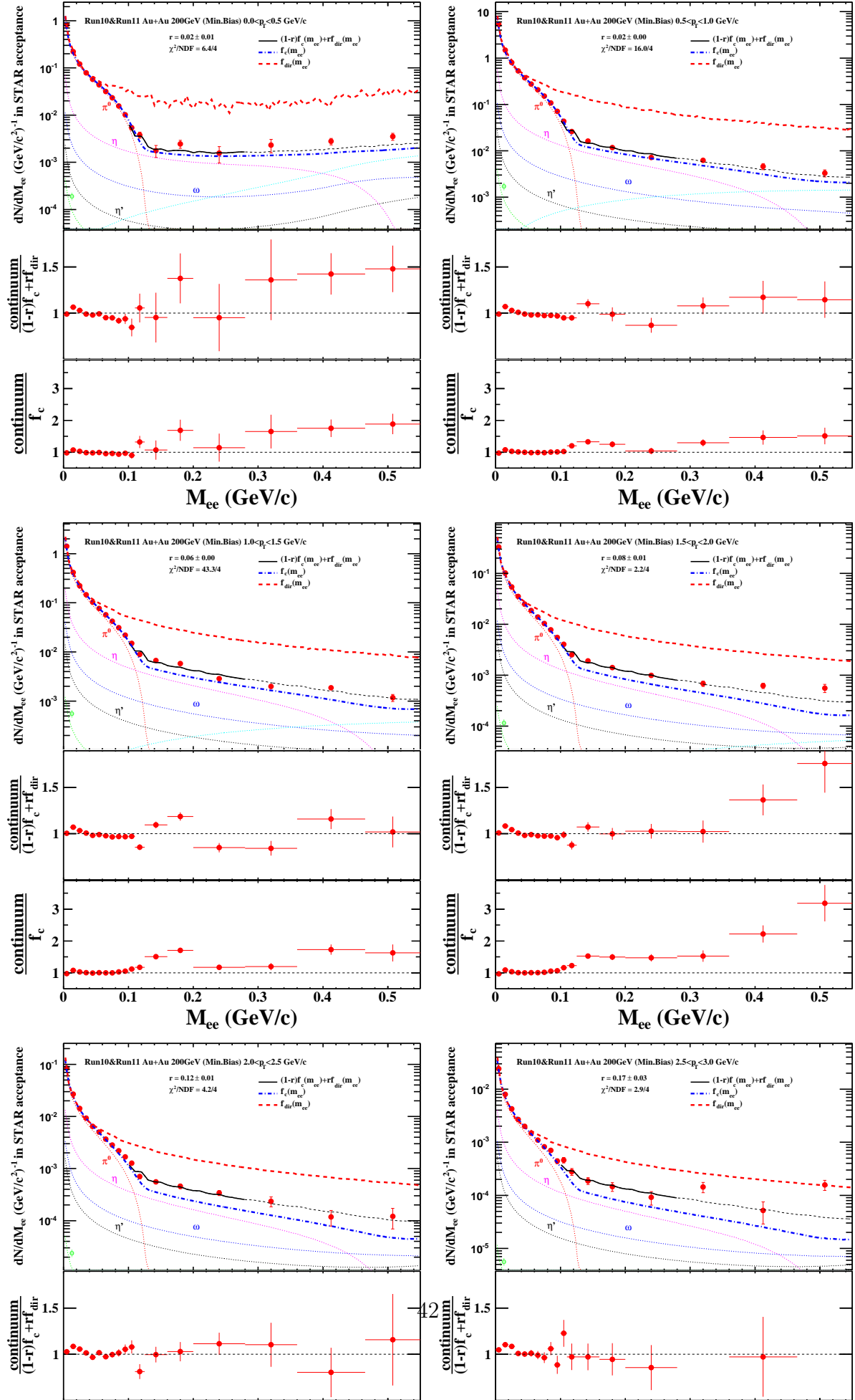


Figure 0.46: The $L(M_{ee})/M_{ee}$ shapes smeared by the STAR acceptance. The p_T dependence of STAR acceptance can be observed in low p_T .

Fig. 0.47 shows the two components ($f_c(M_{ee})$ and $f_{dir}(M_{ee})$) together with a fit result for Run10 and Run11 combined spectra. The error bars in the plots are the combination of the statistical errors and the systematic errors for the di-electron continuum. This means all systematic uncertainty contribution sources are considered in the direct virtual photon extraction. They are included in the fitting uncertainties which will be propagated into the statistical uncertainty in direct virtual photon yield. This systematic error will be discussed in Sec. 0.8. The dashed (black) curve at greater M_{ee} shows the fit function outside of the fit range in both figures.

The fitting results getting from Fig. 0.47 are set as the default value for further systematic uncertainty study.

The bottom two panels in Fig. 0.47 and Fig. 0.48 show the ratio of di-electron continuum over the total fit function and the ratio of di-electron continuum over the normalized cocktail in different p_T slices. In the range with good statistics, the ratio of di-electron



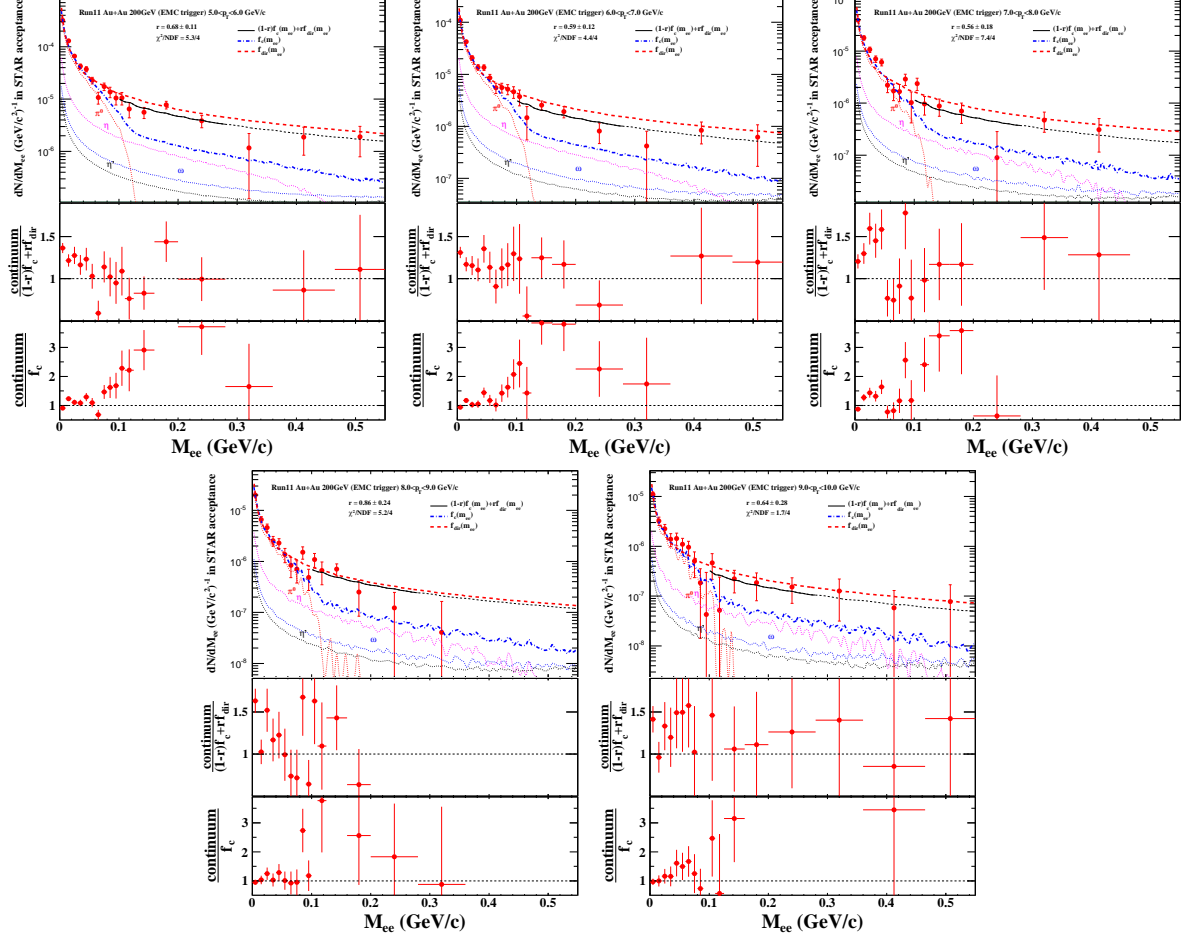


Figure 0.48: The two component function fit on Run11 Au+Au di-electron continuum in $0.1 < M_{ee} < 0.28$ GeV/ c^2 at 200GeV with EMC triggered events in high p_T . The errors shown are the quadrature sum of statistical and systematic errors. The bottom panels are the ratio of data points versus fit function and the data points versus normalized cocktail.

continuum over the total fit function is consistent with 1 within in errors.

The fraction for direct virtual photon which stands for the ratio of direct virtual photon versus inclusive photon is obtained from the two-components fitting. Fig. 0.49 shows the fraction compared with the next-to-leading-order perturbative QCD (NLO pQCD) calculation.

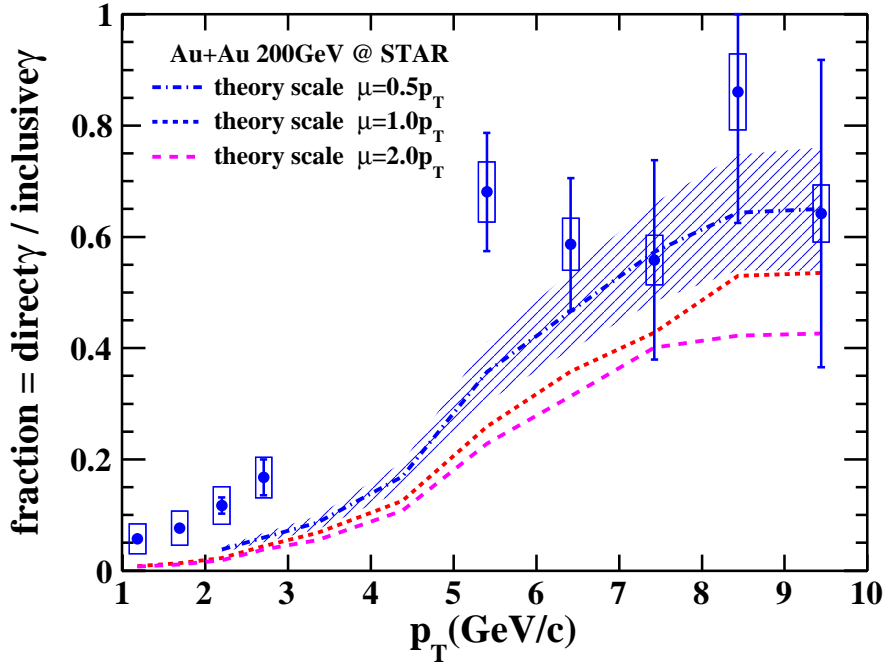


Figure 0.49: The fraction of direct virtual photon compared with the NLO pQCD prediction. The curves represent $T_{AA}d\sigma_{\gamma}^{NLO}(p_T)/dN_{\gamma}^{inclusive}(p_T)$. The red and blue curves corresponds to the theory scale $\mu = 0.5p_T$, $1.0p_T$, respectively, showing the scale dependence of the theory.

0.7.4 Direct virtual photon invariant yield

From Eq. 0.13 and Eq. 0.15, the direct virtual photon contribution used for fitting can be written as Eq. 0.16. Based on this equation, the direct virtual photon invariant yield can be calculated as Eq. 0.17.

$$r \times F \times \left(\frac{L(M)}{M} \right) = \frac{d^2 N_{ee}}{dM} = \frac{2\alpha}{3\pi} \frac{L(M)}{M} dN_{\gamma} \quad (0.16)$$

$$\frac{d^2N_\gamma}{2\pi p_T dp_T dy} = \frac{r \times F / (\frac{2\alpha}{3\pi})}{2\pi p_T dp_T dy} \quad (0.17)$$

A T_{AA} scaled fit function modified by PHENIX 200 GeV $p + p$ cross section is used for comparison. Fig. 0.50 left panel shows this comparison. For $p_T > 5$ GeV/ c , the direct virtual photon invariant yield follows the T_{AA} scaled $p + p$ cross section within uncertainties (fit function modified by $p + p$ cross section / 42 (mb) $\times N_{coll}^{STAR}$) which indicates a dominant contribution from the primordial step of hard parton scattering. In the p_T range $1 < p_T < 5$ GeV/ c , an excess of direct virtual photon compared to T_{AA} scaled $p + p$ cross section is observed. The green band in the plot indicates the uncertainty of the pp reference. It consists of uncertainties from pp fitting and N_{coll} . The relative uncertainty of N_{coll} is smaller in most central, so the relative uncertainty of pp reference is also smaller in most central. A theoretical calculation from private communication with Ralf Rapp is also used for comparison. Fig. 0.50 right panel shows this comparison. Within uncertainties, the direct virtual photon invariant yield is consistent with the sum of QGP, hadron gas and primordial contribution.

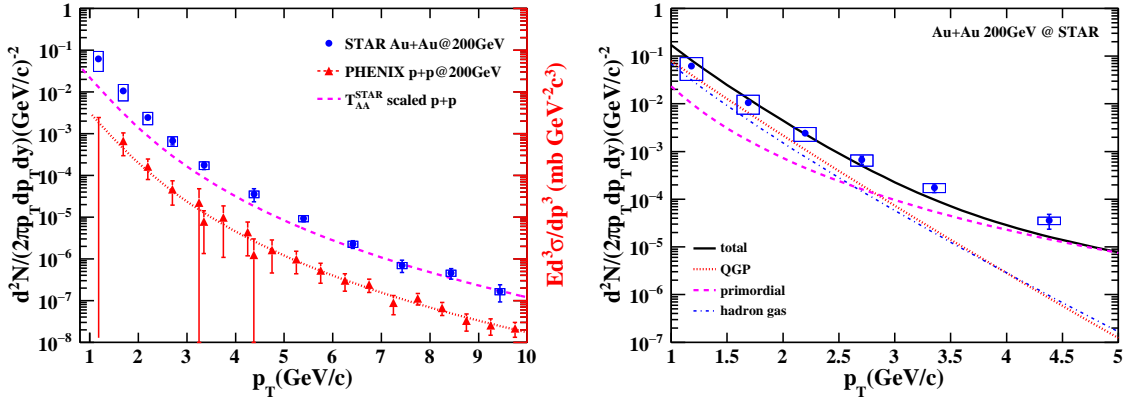


Figure 0.50: The invariant yield of direct virtual photon in 0-80%. The pink dashed curve represents a power-law fit to PHENIX 200GeV $p + p$ cross section, scaled by T_{AA} . Right panel shows the direct virtual photon invariant yield compared to model predictions including the contributions from different sources.

Fig. 0.51 shows the direct virtual photon invariant yield in different centralities. The significant deviation between 3-5GeV/ c is caused by the low purity and statistics. Fig. 0.53 shows a centrality differential direct virtual photon invariant yield. The data points are

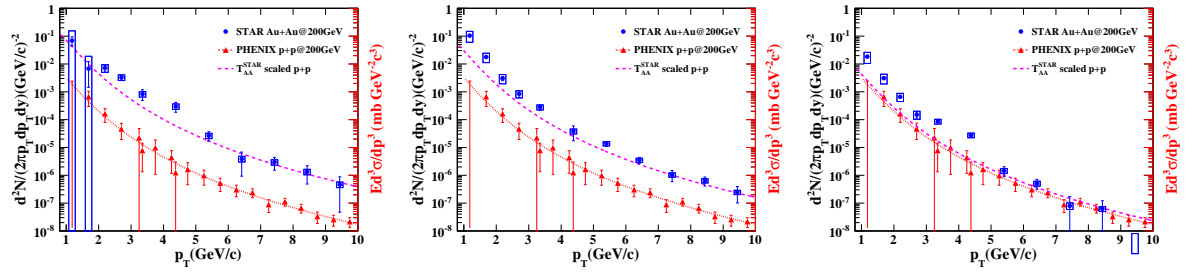


Figure 0.51: The invariant yield of direct virtual photon. The pink dashed curve represents a power-law fit to PHENIX 200GeV $p + p$ cross section, scaled by T_{AA} . Left: 0-10%. Middle: 10-40%. Right: 40-80%.

scaled by different factors for clarification.

Figure 0.54 shows the comparison of the data from STAR, PHENIX, and the theoretical model calculations. Panel (a) is the excess yield, which is the direct photon yield with the N_{coll} scaled $p+p$ contribution subtracted, in comparison with the thermal component contributions in the model calculations.

0.8 Systematic Uncertainty

For the analysis range is in low mass region, the systematic uncertainty is studied only in the like-sign method region ($M_{ee} < 0.7$ GeV/c). The systematic uncertainties come from two main parts.

1. The uncertainty from di-electron continuum
2. The uncertainty from the fitting method

0.8.1 Uncertainty from di-electron continuum

The following bullets show the contributed sources for the uncertainty from di-electron continuum.

1. photon conversion rejection uncertainty
2. Uncertainty from the acceptance correction for like-sign pair
3. Detection efficiency and acceptance uncertainty

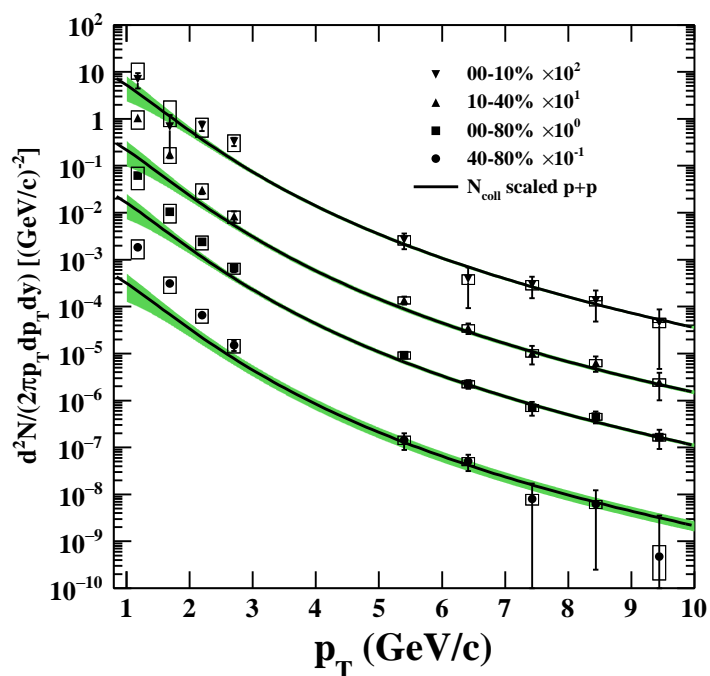


Figure 0.52: Centrality dependence of the direct photon invariant yields as a function of p_T in Au+Au collisions at $\sqrt{s_{NN}} = 200$ GeV. The solid curve represents a power-law fit to PHENIX 200 GeV $p + p$ cross section, scaled by T_{AA} , including a green band which explain the uncertainty contributed from fitting and T_{AA} scale. The error bars and boxes represent the statistical and systematic uncertainties, respectively.

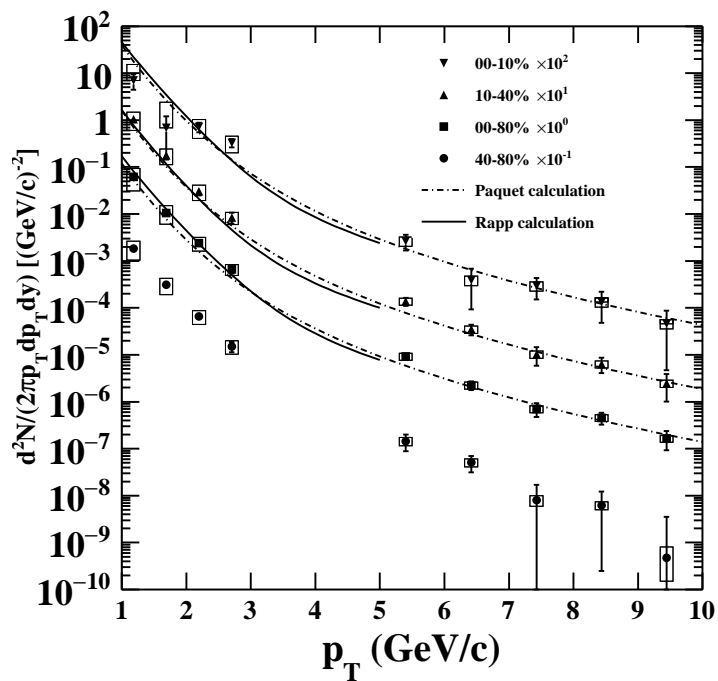


Figure 0.53: The direct photon invariant yields as a function of p_T in Au+Au collisions at $\sqrt{s_{NN}} = 200$ GeV compared to model predictions from Rapp et al. and Paquet et al. The statistical and systematic uncertainties are shown by the bars and boxes, respectively.

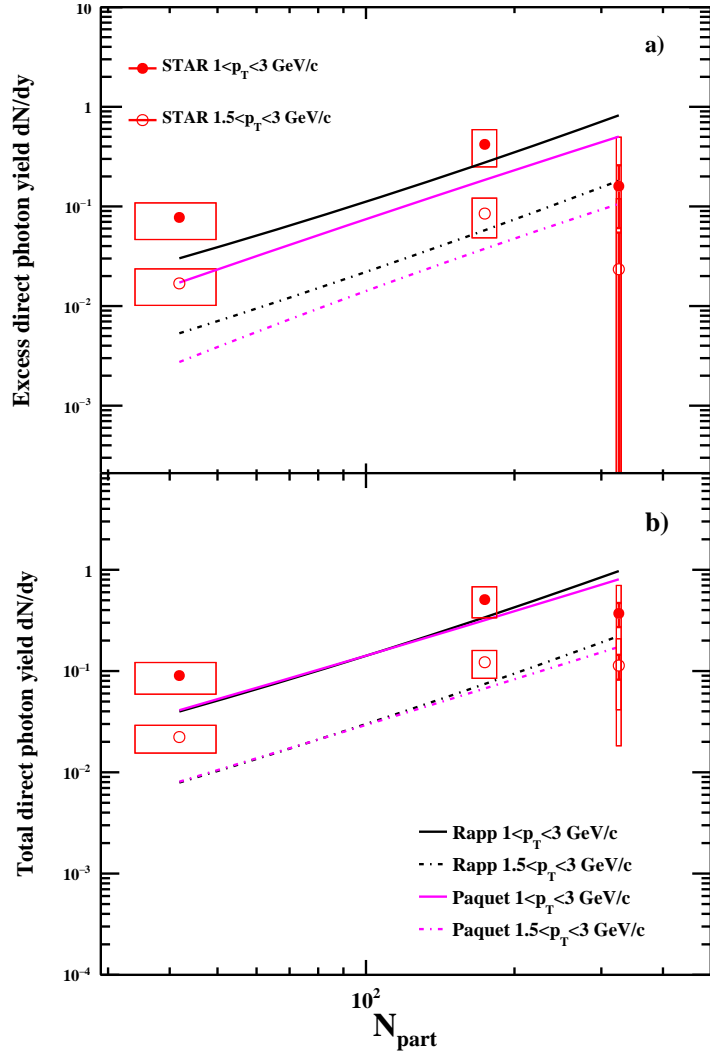


Figure 0.54: The comparison of the data from STAR, PHENIX, and the theoretical model calculations. Panel (a) is the excess yield, which is the direct photon yield with the N_{coll} scaled p+p contribution subtracted, in comparison with the thermal component contributions in the model calculations.

4. Difference between Run10 and Run11

The photon conversion rejection (ϕ_V cut) is applied to both π^0 embedding sample and virtual photon decay sample. The difference between these two results is parameterized by a constant which is 3%. This 3% is set as the uncertainty from photon conversion rejection.

For the uncertainty from acceptance correction between unlike-sign and like-sign electron pairs, considering the source of this uncertainty, the acceptance factor (Eq. 0.4) difference between full magnetic field (FF) and reversed full magnetic field (RFF) is considered as the main contributed source. The relative uncertainty from this source can be calculated by taking the ratio of the relative acceptance factor uncertainty over the like-sign signal over background ratio.

The uncertainty of the pair detection efficiency is a overall value without p_T and mass dependence. This uncertainty is set to 13% for Run10 and 14.6% for Run11 based on the relative di-electron study for Au+Au 200GeV MB data at STAR. Since it is a overall uncertainty without any mass and p_T dependence, this efficiency correction uncertainty is only included in the direct virtual photon invariant yield but not included in the fraction(two-component fitting).

There are some differences between Run10 and Run11 continuum in different centralities bins. Fig. 0.44 shows a constant fitting to these differences. The fitting results are set as a systematic uncertainty contribution.

0.8.2 Uncertainty from the fitting method

Two sources are considered as the main uncertainty contribution sources from the fitting method. One is the uncertainty of the cocktail and the other is the uncertainty caused by the fitting range.

0.8.2.1 Uncertainty from fitting range

To get the uncertainty from the fitting range, the results from fitting range $0.08 < M_{ee} < 0.28 \text{ GeV}/c^2$, $0.12 < M_{ee} < 0.28 \text{ GeV}/c^2$ and $0.10 < M_{ee} < 0.36 \text{ GeV}/c^2$ are generated. A linear fitting to the differences between these results and the default value describes the contribution from fit range in systematic uncertainty. These fitting plot can be found in Fig. 0.55. The relative uncertainty from this source can be found in Fig. 0.57.

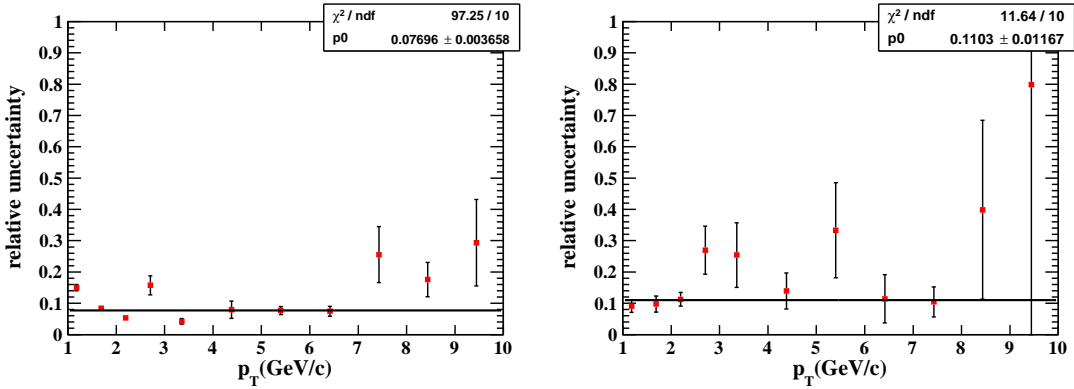


Figure 0.55: Uncertainty contribution from fit range. Left: 0-80%. Right: 0-10%

0.8.2.2 Input p_T spectra uncertainty

As the cocktail is used for the two components fitting, its uncertainty especially the π^0 and η sources will impact the fraction and yield significantly. The excess will increase with increased π^0 and decreased η contribution. From Tab. 0.4, the uncertainty of rapidity density dN/dy for π^0 and η is 8% and 30%, respectively. As mentioned in Sec. 0.5.1, a TBW model fitting to published data is used as the input p_T shape. For η source, since there is no low p_T measurements, the p_T shape in low p_T range for η is only the model prediction. To quantify the uncertainty from η , several p_T input sets below are used.

- a. TBW p_T input, artificially set the parameter $\beta = 0.5$ below 2 GeV/c, scale the p_T spectra below 2 GeV/c to touch the default value at 2 GeV/c.
- b. TBW p_T input, artificially set the parameter $\beta = 0.3$ below 2 GeV/c, scale the p_T spectra below 2 GeV/c to touch the default value at 2 GeV/c.

c. TBW p_T input, give +30% overall shift.

d. TBW p_T input, give -30% overall shift.

Sets a. and b. are for the uncertainty below 2 GeV/c. Sets c. and d. are for the uncertainty from the precision on η measurement. Fig. 0.56 shows the distributions from these sets compared to the default values.

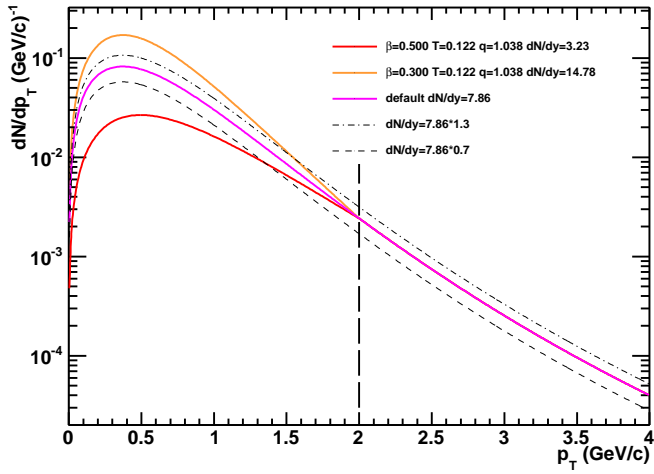


Figure 0.56: The p_T distributions from different sets compared to the default value for η source in cocktail simulation.

The maximum relative uncertainty which is the maximum relative difference between the results from these sets and the default value is used to compare with the difference of direct virtual photon yield between "Scale" and "Integral" dN/dy . The larger one is set as the uncertainty from η . For π^0 uncertainty, similar method is used. The p_T input is shifted $\pm 8\%$ to calculate the uncertainty. For charm contribution, its cross section is 0.8 ± 0.36 . This uncertainty is also considered by similar method. Fig. 0.57 and Fig. 0.58 show the relative uncertainties for all these sources in different centralities. The detail numbers are listed from Tab. 0.6 to Tab. 0.9

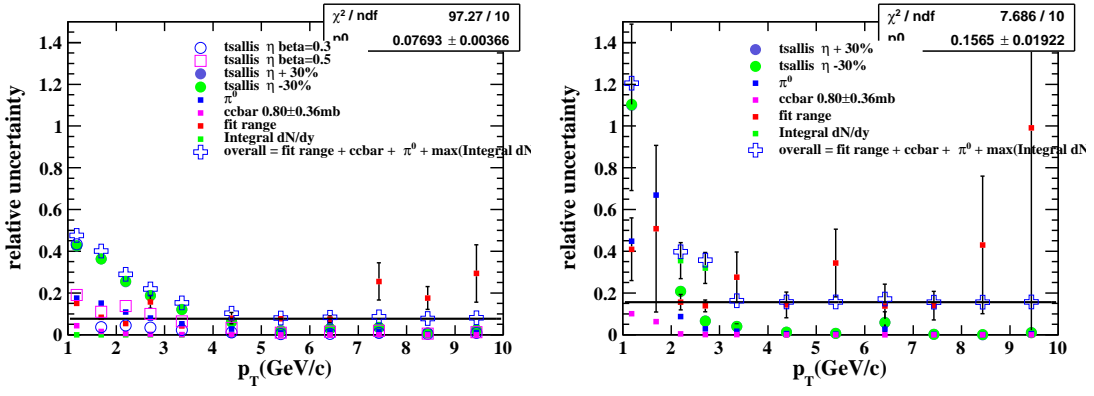


Figure 0.57: The relative uncertainty and its contributed sources. Left: 0-80%. Right: 0-10%

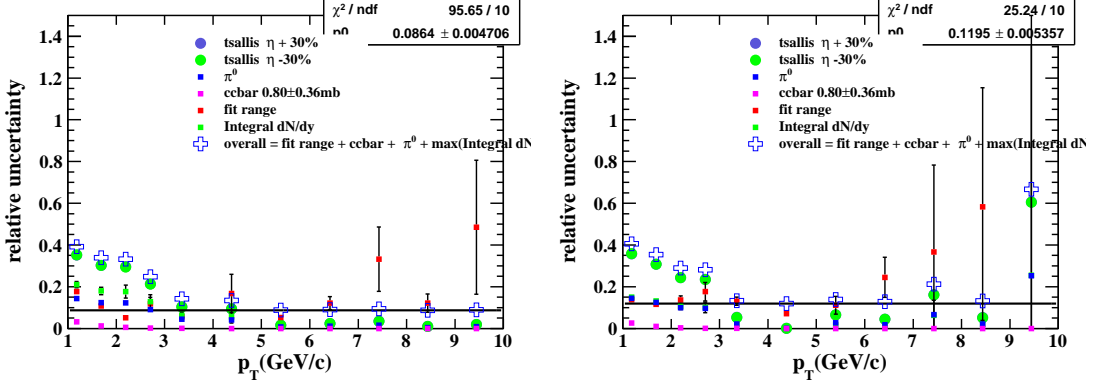


Figure 0.58: The relative uncertainty and its contributed sources. Left: 10-40%. Right: 40-80%

Table 0.6: Systematic uncertainties from different sources in 0-80%.

p_T	fit range(%)	pi0(%)	cc(%)	eta(%)	RunDiff (%)	Eff(%)	total(%)
1.18042	7.69339	17.537	4.30941	43.2901	2.214	14.6	49.7735
1.68877	7.69339	15.0884	1.61813	36.3383	2.214	14.6	42.7551
2.19699	7.69339	10.8526	0.479347	25.6506	2.214	14.6	32.4533
2.70434	7.69339	8.04469	0.127267	18.8271	2.214	14.6	26.3902
3.35383	7.69339	5.29039	0.0282865	12.1009	2.214	14.6	21.2525
4.38091	7.69339	2.76233	0.00430506	6.20562	2.214	14.6	17.9831
5.40048	7.69339	0.861528	0.000734341	1.89298	2.214	14.6	16.7802
6.41482	7.69339	1.34322	0	2.99198	2.214	14.6	16.9707
7.42615	7.69339	1.57507	0	3.53732	2.214	14.6	17.0951
8.43469	7.69339	0.35082	0.0055778	0.845385	2.214	14.6	16.676
9.44118	7.69339	1.07574	0	2.30543	2.214	14.6	16.8441

Table 0.7: Systematic uncertainties from different sources in 0-10%.

p_T	fit range(%)	pi0(%)	cc(%)	eta(%)	RunDiff (%)	Eff(%)	total(%)
1.18042	15.6522	44.8377	10.0903	110.37	5.5	14.6	121.582
1.68877	15.6522	66.8753	6.2924	242.258	5.5	14.6	252.367
2.19699	15.6522	8.75075	0.365144	35.522	5.5	14.6	42.7425
2.70434	15.6522	2.81335	0.0501641	31.9572	5.5	14.6	38.9561
3.35383	15.6522	1.73087	0.0108896	3.95425	5.5	14.6	22.5174
4.38091	15.6522	0.543796	0.00146182	1.59192	5.5	14.6	22.1638
5.40048	15.6522	0.289335	0.00045368	0.646835	5.5	14.6	22.1112
6.41482	15.6522	2.65818	0	6.28942	5.5	14.6	23.1306
7.42615	15.6522	0.132371	0	0.30856	5.5	14.6	22.1024
8.43469	15.6522	0.0502454	0.00579755	0.100491	5.5	14.6	22.1001
9.44118	15.6522	0.577414	0	1.02297	5.5	14.6	22.131

Table 0.8: Systematic uncertainties from different sources in 10-40%.

p_T	fit range(%)	pi0(%)	cc(%)	eta(%)	RunDiff (%)	Eff(%)	total(%)
1.18042	8.63989	14.3345	3.13152	35.3052	2.9715	14.6	41.933
1.68877	8.63989	12.4284	1.20888	30.26	2.9715	14.6	36.9896
2.19699	8.63989	12.2759	0.48521	29.602	2.9715	14.6	36.3848
2.70434	8.63989	9.01614	0.134794	21.3655	2.9715	14.6	28.8865
3.35383	8.63989	4.48076	0.0234576	10.3755	2.9715	14.6	20.6001
4.38091	8.63989	4.14156	0.00686935	9.42212	2.9715	14.6	20.0641
5.40048	8.63989	0.709923	0.000833406	1.56166	2.9715	14.6	17.3084
6.41482	8.63989	1.05901	0	2.38352	2.9715	14.6	17.4195
7.42615	8.63989	1.51342	0	3.47933	2.9715	14.6	17.6362
8.43469	8.63989	0.421981	0.00252037	0.996025	2.9715	14.6	17.2571
9.44118	8.63989	0.888995	0	1.9379	2.9715	14.6	17.3546

Table 0.9: Systematic uncertainties from different sources in 40-80%.

p_T	fit range(%)	pi0(%)	cc(%)	eta(%)	RunDiff(%)	Eff(%)	total(%)
1.18042	11.9477	14.4637	2.55579	35.8928	1.952	14.6	43.1711
1.68877	11.9477	12.4746	1.00933	30.8175	1.952	14.6	38.2893
2.19699	11.9477	9.92068	0.322836	24.373	1.952	14.6	32.439
2.70434	11.9477	9.61366	0.116258	23.5326	1.952	14.6	31.7165
3.35383	11.9477	2.17884	0.00767917	5.31424	1.952	14.6	19.8168
4.38091	11.9477	0.0149596	0	0.0578438	1.952	14.6	18.9663
5.40048	11.9477	2.676	0.00113067	6.5279	1.952	14.6	20.2359
6.41482	11.9477	1.8457	0	4.44107	1.952	14.6	19.5665
7.42615	11.9477	6.65306	0	16.2235	1.952	14.6	25.8299
8.43469	11.9477	2.10396	0.00743873	5.20927	1.952	14.6	19.7808
9.44118	11.9477	25.2952	0	60.5683	1.952	14.6	68.3233